• U C •
FCTUC FACULDADE DE CIÊNCIAS E TECNOLOGIA
UNIVERSIDADE DE COIMBRA

DEPARTAMENTO DE ENGENHARIA MECÂNICA

Thermomechanical Modelling of the Draw Bead test

Submitted in Partial Fulfilment of the Requirements for the Degree of Master in Mechanical Engineering in the speciality of Production and Project

Modelação termomecânica do ensaio de freio

Author
Miguel Pais Costa

Advisors
Diogo Mariano Simões Neto
Marta Cristina Cardoso de Oliveira

Jury

President	**Professor Doutor Pedro André Dias Prates** **Professor Auxiliar Convidado da Universidade de Coimbra**
Vowel	**Professor Doutor José Luís de Carvalho Martins Alves** **Professor Associado da Universidade do Minho**
Advisor	**Professor Doutor Diogo Mariano Simões Neto** **Professor Auxiliar Convidado da Universidade de Coimbra**

Coimbra, June, 2017

“The important thing is not to stop questioning. Curiosity has its own reason for existing. One cannot help but be in awe when he contemplates the mysteries of eternity, of life, of the marvellous structure of reality. It is enough if one tries merely to comprehend a little of this mystery every day. Never lose a holy curiosity.”

Albert Einstein

ACKNOWLEDGEMENTS

My academic path wouldn't have been possible without the guidance, sacrifice and unconditional support of my family, especially my Mother, Francisco and my Grandmother, to whom I dedicate this thesis, for having given everything they could and sometimes what they couldn't so that I could embrace this challenge.
I can’t thank you enough.

The biggest thank you goes to my advisors, Professor Diogo Mariano Simões Neto and Professor Marta Cristina Cardoso de Oliveira, for the dedication, motivation and support that helped me get through all the work. Thank you for taking your time and knowledge to answer all my questions and doubts. It has been a pleasure working with you. Similarly, I have to thank the entire staff of the research room, for being able to keep a light and relaxed environment during the long days spent working.

Mariana, thank you for the support, comfort and care that kept me focused throughout the last two years. Thank you for the patience and character to endure my not-so-good days, which, I know, it’s never been a simple task.

Last but not least, I want to thank my great friends and colleagues that have accompanied me since day one. André Adaixo and Gonçalo Oliveira, thank you for your friendship even in the darkest days. Also, João Melo, Sébastien Silva, Rita Sousa, Adriana Garcia, Miguel Brito and Miguel Sousa, thank you for all the moments shared throughout the years.

This work was carried out under the project “Improving the manufacturing of metallic bipolar plates for fuel cells using the rubber forming process” with reference P2020-PTDC/EMS-TEC/0702/2014 (POCI-01-0145-FEDER-016779) and project “Watch4ming: Monitoring the stamping of advanced high strength steels” with reference P2020-PTDC/EMS-TEC/6400/2014 (POCI-01-0145-FEDER-016876), both co-funded by the Foundation for Science and Technology and the EU/FEDER, through the program COMPETE 2020.

Abstract

Nowadays, advanced high-strength steels (AHSS) are used in stamping processes particularly due to their good strength-to-weight ratio. However, the high strength also leads to the necessity of improved knowledge concerning the heat generated by plastic deformation and contact with friction, since this can be a determining factor for the correct description of a given forming process. In this context, the numerical simulations of stamping processes involve solving not only the mechanical problem, but also the thermal problem.

The main objective of this work is the numerical study of the contact with friction conditions involved in the draw bead test, with particular focus on the thermal problem. To achieve this goal, a thermomechanical test model was built, considering both the heat transfer to the tools (IHTC) and for the environment. The effects of the main parameters of process are analysed, in particular the penetration of the punch, the side clearance between the tools, the coefficient of friction, the mechanical properties of the material of the blank and the pulling speed of the grip. In addition to the temperature evolution, also the forces, stresses, strains, contact angles and springback were studied.

For the geometrical conditions under analysis, the deformation in the width direction is residual, which allows the use of a model that assumes plane strain conditions, significantly reducing the computational costs. For the studied configurations, the parameter that had the greater influence on the blank temperature is the pulling speed of the grip, followed by the penetration of the punch and the side clearance. On the other hand, the parameter that presented the lower influence on the temperature of the blank was the friction coefficient, being almost negligible to this analysis. The forces are especially influenced by the coefficient of friction, while the contact angles depend mainly on the penetration of the punch.

Keywords Numerical Simulation, Draw Bead Test, Thermomechanical problem, IHTC, Heat generated by plastic deformation and friction.

Resumo

Hoje em dia os aços de alta resistência são muito utilizados em processos de estampagem graças à boa relação resistência-peso. No entanto, devido à sua elevada resistência mecânica, é necessário melhorar o conhecimento acerca do calor gerado por deformação plástica e por atrito, uma vez que este pode ser um fator determinante para a correta descrição do processo em causa. Neste contexto, a simulação numérica de processos de estampagem envolve a resolução não só do problema mecânico, mas também do problema térmico.

O principal objetivo deste trabalho é o estudo numérico das condições de contacto com atrito presentes no ensaio de freio (*draw bead test*), em particular da componente térmica do problema. Para tal, foi construído um modelo termomecânico do ensaio, considerando tanto a transmissão de calor para as ferramentas (IHTC) como para o meio ambiente. Neste trabalho, é analisado o efeito dos principais parâmetros do processo, nomeadamente a penetração do punção, a folga lateral entre as ferramentas, o coeficiente de atrito, as propriedades mecânicas do material da chapa e a velocidade da amarra. Para além da evolução da temperatura, são estudadas as forças, tensões, deformações, ângulos de contacto e retorno elástico.

Para as condições geométricas em análise, a deformação na direção da largura é residual, o que permite a adoção de um modelo que assume condições de estado plano de deformação, o que permite reduzir de forma significativa o custo computacional. Para as configurações estudadas, o parâmetro que revelou maior influência na temperatura da chapa foi a velocidade da amarra, seguida da penetração do punção e da folga lateral. Por outro lado, o parâmetro que menos influenciou a temperatura da chapa foi o coeficiente de atrito, que apresenta um efeito negligenciável. As forças são especialmente influenciadas pelo coeficiente de atrito, enquanto que os ângulos de contacto dependem principalmente da penetração do punção.

Palavras-chave: Simulação numérica, Ensaio de freio, Problema termomecânico, IHTC, Calor gerado por deformação plástica e atrito

Contents

List of Figures

List of Tables

Nomenclature

The symbols used in this thesis are presented in this section, separated into Greek and Roman category. Throughout this text, reference is given to the use of compact tensor notation, where no indices are used to represent mathematical entities.

Roman symbols

$\mathbf{C}$	Capacity matrix
c	Specific heat capacity
$\mathbf{D}^{\mathrm{p}}$	Plastic strain rate
E	Young's modulus
F, G, H, L, M, N	Anisotropy parameters of the Hill'48 yield criterion
$\mathbf{f}$	Vector of prescribed flows and boundary terms relative to the environment and the arbitrary obstacle
G_{x}	Grip force in the x-direction
$G_{\mathrm{d+f}}$	Grip force in the x-direction under frictional conditions
G_{d}	Grip force in the x-direction funder frictionless conditions
g	Side clearance between the punch and the dies;
g_{a}	Gravitational acceleration
g_{n}	Nominal gap distance between the blank and the tools
$\dot{\mathbf{g}}_{\mathrm{t}}$	Tangential slip velocity
$\bar{h}$	Average heat transfer coefficient (HTC) to the environment
h_{conv}	Convection coefficient
h_{c}	Interfacial heat transfer coefficient (IHTC)
h_{int}	Evolving interfacial heat transfer coefficient
h_{rad}	Radiation coefficient
h_{sup}	Upper interfacial heat transfer coefficient threshold value
$\mathbf{K}$	Conductivity matrix
K	Constitutive parameter of Swift's hardening law

$\mathbf{k}$	Thermal conductivity vector
k	Thermal conductivity
L	Average length of the heat transfer area
m	Parameter controlling the increase rate of interfacial heat transfer coefficient
n	Parameter of the Swift's hardening law
$\overline{Nu}_{\mathrm{L}}$	Average Nusselt number
$\mathbf{n}$	Normal vector to the boundary surface
p	Punch penetration
P_{d}	Punch force in the *z*-direction under frictionless conditions
$P_{\mathrm{d+f}}$	Punch force in the *z*-direction under frictional conditions
p_{f}	Full punch penetration
P_{x}	Punch force in the *x*-direction
P_{z}	Punch force in the *z*-direction
Pr	Prandtl number
$\mathbf{Q}$	Vector of nodal heat flux input
q_{frict}	Heat flux due to the frictional contact
$\bar{q}$	Imposed heat flux at Neumann boundary condition
q	Internal heat generation per unit volume
R	Radius of the tools
Ra_{L}	Rayleigh number
r_0	Anisotropy coefficient from the uniaxial tensile test at the rolling direction
r_{45}	Anisotropy coefficient from the uniaxial tensile test at 45° with the rolling direction
r_{90}	Anisotropy coefficient from the uniaxial tensile test at the transverse direction
r_{φ}	Anisotropy coefficient from the uniaxial tensile test at the direction φ
$\overline{T}$	Imposed temperature on the surface of Ω
T_0	Initial temperature for the open set Ω
T_{∞}	Environment temperature

T_f	Average temperature
T_{obs}	Isothermal obstacle temperature
T_r	Radiation surface temperature
T_s	Blank surface temperature
T', T_r'	Absolute temperatures of the surface γ_{R_2}
t	Time instant
t_0	Blank initial thickness
$\mathbf{t}_t$	Friction force
U	Global heat transfer coefficient
R_t''	Thermal contact resistance
Y_0	Yield stress

Greek symbols

α	Thermal diffusivity
β	Volumetric thermal expansion coefficient
γ	Boundary surface
γ_c	Thermal contact boundary condition
γ_D	Dirichlet boundary condition
γ_N	Neumann boundary condition
γ_{R_1}, γ_{R_2}	Robin boundary conditions
Δt	Time increment
ε_0	Parameter of the Swift's hardening law
$\bar{\varepsilon}^p$	Equivalent plastic strain (EPS)
η	Total amount of heat dissipated to the solid body
θ_1	Contact angle between the Blank and the Left Die
θ_2	Contact angle between the Blank and the Punch
θ_3	Contact angle between the Punch and Right Die
θ_{2D}	Springback angle of the 2D model
θ_{3D}	Springback angle of the 3D model
κ_r	Radiation parameter

Λ	Time integration method
μ	Friction coefficient
μ_p	Predicted friction coefficient
ν	Kinematic viscosity
ξ	Fraction of generated energy converted into heat
ρ	Mass density
$\boldsymbol{\sigma}$	Cauchy stress tensor
σ_{11}	Normal stress in relation to the rolling direction
φ	Angle with respect to the rolling direction
χ	Taylor-Quinney factor
Ω	Isothermal obstacle with arbitrary shape

Acronyms

2D	Two Dimensional
3D	Three Dimensional
AHSS	Advanced High Strength Steel
DD3IMP	Deep Drawing 3D IMPlicit finite element code
EPS	Equivalent Plastic Strain
FE	Finite Element
GP	Gauss Point
HTC	Heat Transfer Coefficient
IHTC	Interfacial Heat Transfer Coefficient
LD	Left Die (cylinder)
P	Punch (cylinder)
RD	Right Die (cylinder)
S	Support cylinder

1. Introduction

Sheet metal forming is a manufacturing method, which makes use of the metallic material to undergo plastic deformation when subjected to an external force, to obtain components with a certain shape, size, and performance. In stamping processes, the sheet metal, the tools and the stamping equipment are three major factors of the process (Hu et al., 2013). The main advantages of this process consist in the high production rate, low labour costs and large volume production capacities. Although the tooling and equipment can be very expensive, the cost can be easily amortized for high production volumes.

The contact conditions in the sheet-tool interface play a critical role, since friction and deformation-induced heating increase the forming temperature. Due to the higher strength of the AHSS steels, the energy converted into heat resulting from the plastic deformation and frictional contact is also higher. In fact, studies show that 90ºC–120ºC temperatures are common in AHSS production conditions (Wagoner et al., 2009). Higher contact pressures and temperatures in the tool-sheet interface increase the risk of failures, while contributing to the inconsistent forming of AHSS.

Sheet metal forming is used in almost every sector of industrial production, such as automotive (Kang et al., 2004), aircraft (Walczyk et al., 1998) and food industries (Ceretti et al., 2010). Due to the high competitiveness of these industries, methods based on trial-and-error procedures have been gradually replaced by the virtual product conception using numerical simulation (Altan and Tekkaya, 2012a). In fact, the finite element method has emerged as the first numerical tool available for troubleshooting problems involving contact with friction and complex geometries (Francavilla and Zienkiewicz, 1975). The practical objectives of numerical simulation can be compiled into three main groups: time reduction, cost reduction and increase of product quality (Altan and Tekkaya, 2012a). The main modelling requirements for cold stamping are the description of the material behaviour and contact conditions and friction, as well as a failure criterion. Nevertheless, the friction is influenced by the properties of both contacting materials (Nasser et al., 2010), their surface roughness (Lee et al., 2002), temperature, relative velocity and contact pressure (Rhee, 1974).

1.1. Tribological tests

There are several tribological tests developed over the years to assess the frictional contact conditions in sheet metal forming. These tests are mainly used for evaluating lubrication conditions and estimating the friction coefficient. Depending on the type of contact, there are different tribological tests to consider, such as the strip drawing, limiting dome height, twist compression or draw bead tests (see Figure 1.1).

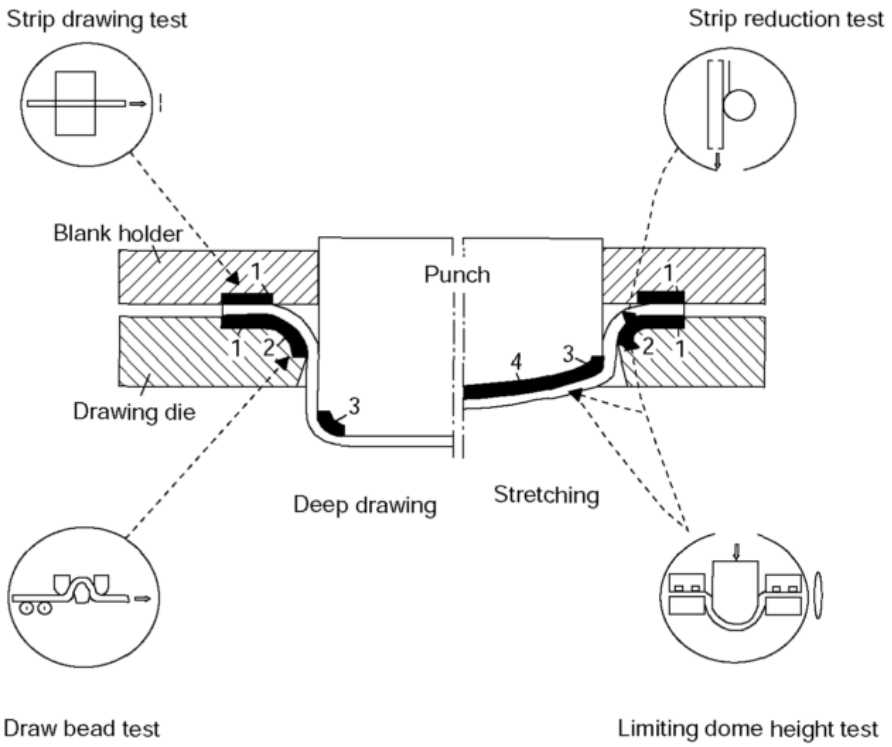

Figure 1.1. Tribological tests used for evaluating lubricants and friction in stamping processes (Altan and Tekkaya, 2012b).

The strip drawing test consists in pulling a blank between two opposing flat dies (performed without deflection of the strip), which are generally wider than the strip. Its main advantage is the simplicity of the test apparatus and the main drawback is that the friction coefficient determined is only valid for flat contact zones, such as the one between the blank holder and the sheet (Dilmec and Arap, 2016). The limiting dome height test comprises a sheet that is clamped by flat die plates and an arbitrary diameter ball that penetrates the sheet until failure occurs. The cup height at failure is taken as the measure of formability and enables the comparison of stamping lubricants and/or coatings (Ayres et al., 1978). The twist

compression test is very used to estimate the friction coefficient for stamping lubricants to apply in different kinds of tool coatings. In this test, a rotating annular tool is pressed against a fixed sheet metal while pressure and torque are measured. The friction coefficient is obtained by from the torque, pressure, mean radius of the tool and the contact area (Altan and Tekkaya, 2012b). In the draw bead test, the general procedure involves pulling a sheet specimen through the draw bead dies and measuring the forces needed to pull the sheet. The test can be performed for frictionless or frictional conditions. Also, the forces and velocities can be changed to emulate the real process conditions. Although these can be considered some of the most used tribological tests to characterize the stamping processes, the contact conditions also depend on the strain paths induced to the blank. In this context, Figure 1.2 illustrates the different tribological tests applicable, depending on the type of contact between tools and blank in a deep drawing operation.

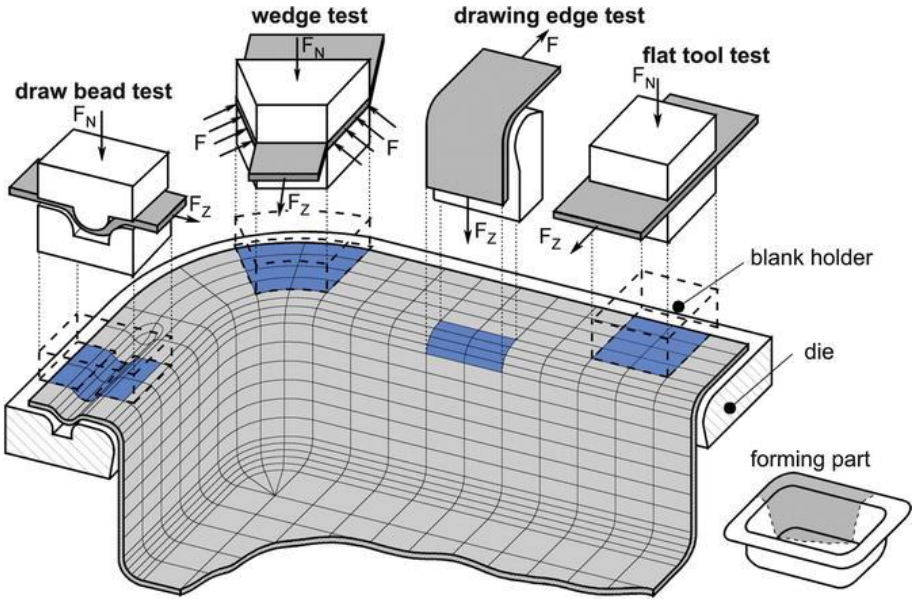

Figure 1.2. Tribological tests suitable for different sections of a deep drawing component (Losch, 2014).

1.2. Objectives of the study and Outline

The main objective of this work is to perform the thermomechanical analysis of the draw bead test using finite element simulation, by studying different configurations of the tools and process conditions. In addition to the process parameters, this study involves the analysis of the temperature evolution considering the heat generated by plastic

deformation and frictional contact and the heat loss by convection to the environment (air) and the tools.

This work is divided in five main chapters. To improve its readability and understanding, this section presents a brief summary of each chapter.

Chapter 1 introduces the subject of the study with a background on the sheet metal forming processes and tribological tests used to evaluate the friction coefficient.

Chapter 2 presents the mechanical set-up of the test, to assess the main geometrical parameters involved in the tools definition and blank spatial location, as well as the main process conditions involved in the draw bead test.

Chapter 3 contains the description of the thermal problem and its finite element formulation. The heat generated by plastic strain and friction, as well as the heat loss by convection and contact with the tools is assessed. In this context, two numerical examples are presented to clarify the finite element formulation of the thermal parameters, namely the interfacial heat transfer coefficient (IHTC) and heat transfer coefficient (HTC).

Chapter 4 presents the results obtained from the numerical simulations of the draw bead test. Firstly, the simpler plane strain conditions hypothesis is explored. Subsequently, the analysis is divided in sub-sections, each evaluating the influence of a specific process parameter, namely: (i) the punch penetration; (ii) the side clearance (lateral distance between the punch and the tools); (iii) the friction coefficient; (iv) the mechanical properties of the material and (v) the pulling speed of the grip; on the parameters that describe the test, such as forces, strains, stresses, temperatures, contact angles and springback.

Chapter 5 contains the main conclusions withdrawn from the study carried out on the previous chapters.

2. Draw bead test

This section contains the mechanical modelling of the draw bead test. The set-up of the test is presented, comprising the dimension and location of the tools, as well as the main variables of the test. Later, the finite element model, including the material mechanical behaviour, blank and tools discretization and process conditions, is presented.

2.1. Set-up dimension

The draw bead test is essentially composed by three tools (cylinders), which are placed to induce plastic deformation on a metallic sheet. The process is divided in two phases: in the first the sheet is bended and in the second it is pulled by a grip. In the present study, one more tool (support) is considered for stability purposes. The tools are cylindrical with 10.5 mm of radius and the dimensions of the blank sheet are 450×25×0.8 mm, as shown in Figure 2.1.

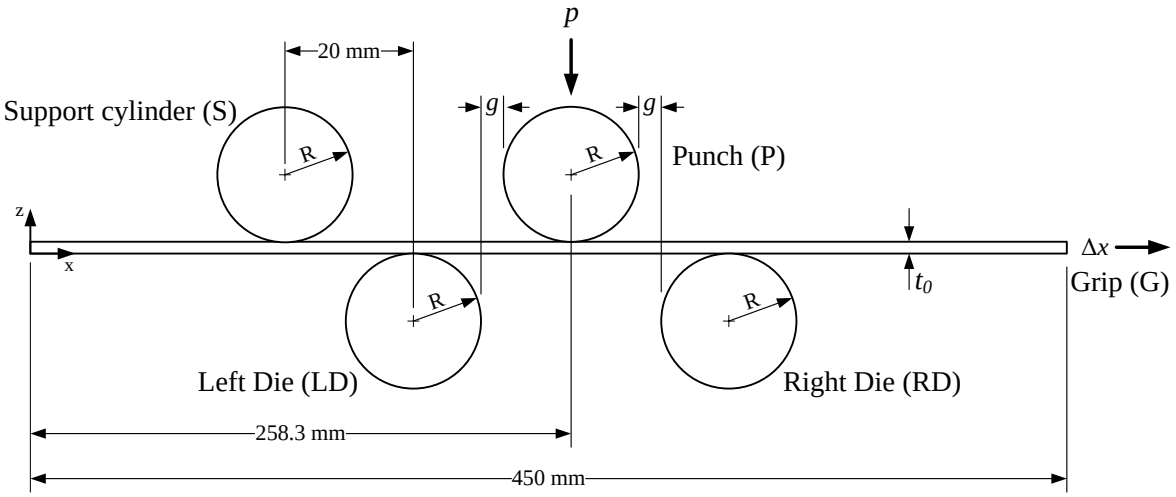

Figure 2.1. Representative scheme of the draw bead test.

In order to simplify the sensibility analysis carried out in Section 4, it is assumed that the position of the punch along the *x*-direction is fixed, while the position of both left and right dies are evaluated from the position of the punch, defining a predefined gap (*g*)

value (see Figure 2.1). In a similar way, the position of the support tool is imposed with respect to the position of the left die. Thus, the fixed initial position of the punch is 258.3 mm in the *x*-direction and 11.3 mm in the *z*-direction, as shown in Figure 2.1. In order to compare different process conditions, some dimensions that define the draw bead test are considered variable in the numerical analysis. The selected variables are the gap distance and the punch penetration, which will be defined in detail in Section 4.

Considering the scheme presented in Figure 2.1, the relationships between the main dimensional parameters, required to calculate all tools positions, are as follows:

$$\begin{aligned} x_{\mathrm{S}} &= x_{\mathrm{LD}} - 20 \\ x_{\mathrm{LD}} &= x_{\mathrm{P}} - 2R - g \\ x_{\mathrm{RD}} &= x_{\mathrm{P}} + 2R + g \ , \end{aligned} \tag{2.1}$$

where x_{S}, x_{LD}, x_{P} and x_{RD} are the support cylinder, left die, punch and right die *x*-coordinates, respectively. R is the tools radius and g is the gap between the punch and the dies. Regarding the horizontal displacement of the grip, it is considered that the blank is pulled at a constant speed, for a fixed value of displacement (150 mm). The influence of the prescribed grip velocity will be discussed further in this work.

2.2. Finite element model

The numerical simulations presented in this work were carried out with the in-house static finite element code DD3IMP (Menezes and Teodosiu, 2000). An updated Lagrangian scheme is used to describe the evolution of the deformation, and in each increment an explicit approach is used to obtain a trial solution of the nodal displacements. Then, the trial solution is corrected by the Newton-Raphson method until an equilibrium configuration is attained. This method is used to resolve the non-linearities associated with the large deformation, the elastoplastic behaviour of the deformable body and the frictional contact, in a single iterative loop. All numerical simulations were performed on a computer machine equipped with an Intel® Core™ i7–4770 K Quad-Core processor (3.5 GHz) and Windows 10 Pro (64-bit platform) operating system.

2.2.1. Material mechanical behaviour

In this work, two different sheet materials are used, both corresponding to dual phase steels (DP500 and D780). The mechanical behaviour of both dual phase sheets is assumed elastoplastic, considering isotropic elastic behaviour and anisotropic plastic behaviour. The elastic behaviour is described by the Hooke's law with a Young's modulus of 210 GPa and a Poisson's ratio of 0.30, for both steels. Regarding the plastic behaviour, the isotropic hardening is described by the Swift's law:

$$Y = K\,(\varepsilon_0 + \bar{\varepsilon}^{\,\mathrm{p}})^n\,, \tag{2.2}$$

where K, ε_0, and n are the material parameters, while $\bar{\varepsilon}^{\,\mathrm{p}}$ denotes the equivalent plastic strain (EPS). The material parameters obtained for the Swift's isotropic hardening law are presented in Table 2.1, for each material. The constitutive model adopted allows to describe the mechanical behaviour accurately, as shown in Figure 2.2, which also highlights the differences between the mechanical behaviour of both steels, showing that the DP780 has a significantly higher yield stress than the DP500. In order to simplify the finite element analysis and due to the lack of experimental results, the mechanical behaviour of both materials is assumed to be temperature and strain rate independent.

Table 2.1. Parameters of the isotropic hardening law for each material (Swift law).

Material	Y_0 [MPa]	K [MPa]	ε_0	n
DP500	349.8	877.45	0.0050	0.1736
DP780	500.7	1319.21	0.0015	0.1490

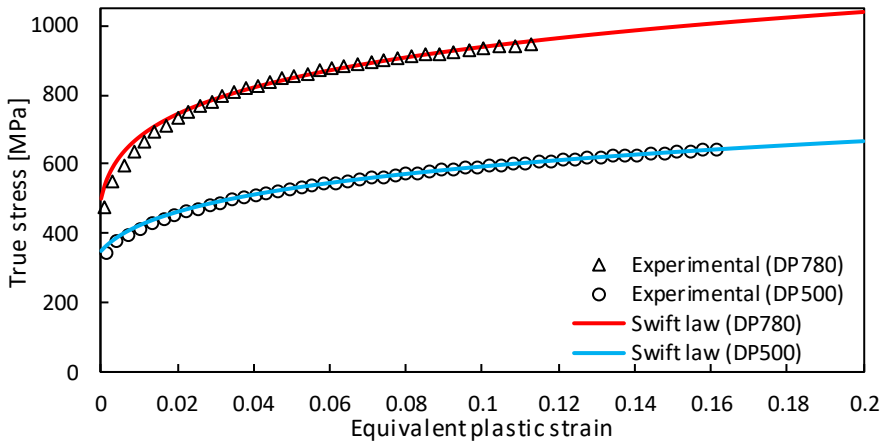

Figure 2.2. Comparison between numerical and experimental stress-strain curves obtained from the uniaxial tensile test at the rolling direction. The hardening behaviour is described by the Swift law

Regarding the plastic anisotropic behaviour, it is described by the (Hill, 1948) yield criterion, for both materials. The anisotropy parameters are determined from experimental *r*-values, evaluated through uniaxial tensile tests performed at three different angles with respect to the rolling direction: 0º, 45º and 90º. Table 2.2 presents the experimental *r*-values for each material.

Table 2.2. Anisotropy coefficients (*r*-values) evaluated at different angles with respect to the rolling direction, for each material.

Material	r_0	r_{45}	r_{90}
DP500	1.02	0.87	1.20
DP780	0.70	1.05	0.88

The anisotropy coefficient at the direction φ as predicted by the Hill'48 yield criterion is defined by:

$$r(\varphi) = \frac{H + (2N - F - G - 4H)\sin^2\varphi\cos^2\varphi}{F\sin^2\varphi + G\cos^2\varphi} = r_\varphi, \tag{2.3}$$

where φ is the angle with respect to the rolling direction, while *F*, *G*, *H* and *N* are the anisotropy parameters of the Hill'48 yield criterion. Considering different angles from the rolling direction, Equation (2.3) can be used to calculate the anisotropy parameters, as follows:

$$H = r_0 G \tag{2.4}$$

$$F = \frac{H}{r_{90}} \tag{2.5}$$

$$N = \frac{1}{2}\frac{(r_0 + r_{90})(2r_{45} + 1)}{r_{90}(r_0 + 1)} \tag{2.6}$$

Considering the condition $G+H=1$:

$$G = \frac{1}{r_0 + 1}, \tag{2.7}$$

which corresponds to the assumption that the hardening law corresponds to the stress-strain curves obtained for the tensile test performed with the specimen cut along the rolling

direction. The four parameters F, G, H and N calculated from Equation (2.3), considering the three different angles with respect to the rolling direction listed in Table 2.2, are presented in Table 2.3 for both metal sheets. It is also assumed that both materials are isotropic in the thickness direction, leading to $L=M=1.5$. The comparison between experimental and predicted anisotropy coefficient distributions is presented in Figure 2.3.

Table 2.3. Hill'48 anisotropy parameters calculated for each material.

Material	F	G	H	L	M	N
DP500	0.421	0.495	0.505	1.500	1.500	1.255
DP780	0.468	0.588	0.412	1.500	1.500	1.637

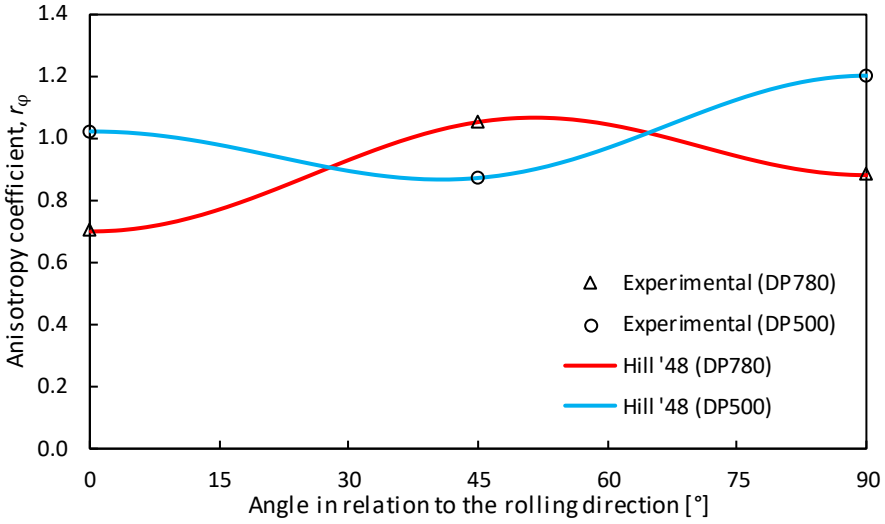

Figure 2.3. Evolution of the coefficient of anisotropy, r_φ, in the plane of the metal sheet, for each material. Comparison between experimental values and Hill'48 yield criterion.

2.2.2. Blank and tools discretization

The numerical model developed in this work considers a deformable body (sheet) in contact with four rigid surfaces (cylinders). Due to material and geometrical symmetry, only half-width of the blank is considered, i.e. a symmetry condition is assumed in the width direction. Two models were studied: a full three dimensional one (3D) and another assuming plane strain conditions in the width direction (2D). The deformable body is discretized with tri-linear isoparametric hexahedral finite elements (FE), associated with a selective reduced integration (SRI) technique.

Due to the draw bead test process conditions, the blank is divided in three zones along the *x*-direction, each having different FE sizes. Figure 2.4 shows the FE zone division in the blank, for both models. This division in zones was considered in order to minimize the computational time without influencing the accuracy of the results. The first zone of the blank, which will be in contact with the tools during the test, is the one with the smaller FE size (0.26 mm) to obtain accurate results. The second zone corresponds to the part of the blank that does not enter in contact with the tools during the test. Thus, the FE size is about 1.5 mm. Finally, the third zone of the blank represents the contact with the grip, which is discretized with only one FE for the whole contact in the length direction. Three FE are considered in the thickness direction in all zones.

When using the two different models it is very important to differentiate the general boundary conditions (symmetry) that are applied in each case. In the 3D model, it is considered that exists symmetry in the plane $y=0$ mm, allowing the simulation of half the blank. In the 2D model, there is one more symmetry condition applied to the plane $y=12.5$ mm, ensuring that the width of the blank does not interfere with the obtained results. The 2D model allows to consider a fewer number of FE in the width direction. In the 3D model a total of 10 FE were considered, while in the 2D model only 2 FE were used[1].The effectiveness of this simpler model will be further discussed in Section 4.1. The entire blank contains 7584 finite elements for the 2D model and 37920 finite elements for the 3D model.

The tools are considered perfectly rigid in the FE model and are modelled by Nagata patches, allowing to describe the 360º angle of their cylindrical shape (Neto et al., 2014). All tools surfaces are composed by 30 Nagata patches, as shown in Figure 2.5. Although the contact between the sheet and the tools occurs only in a part of the cylindrical shape, it is important to model the complete surface (at least of the punch and the dies), to properly take into account the thermal conditions.

[1] It could be only 1 FE in the width direction. However, in order to impose the proper thermal conditions in DD3IMP, the minimum number of elements must be at least 2 FE.

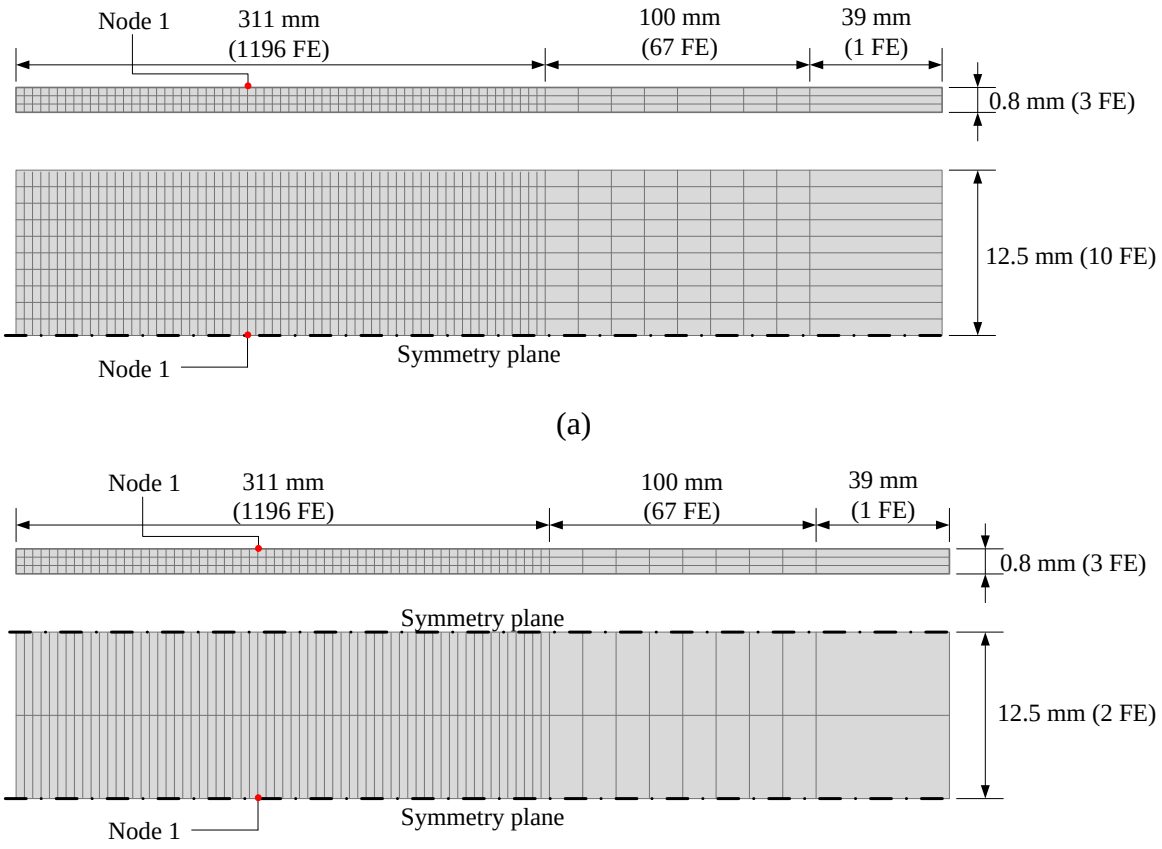

Figure 2.4. Division of the blank in three zones and FE discretization: (a) 3D model; (b) 2D model.

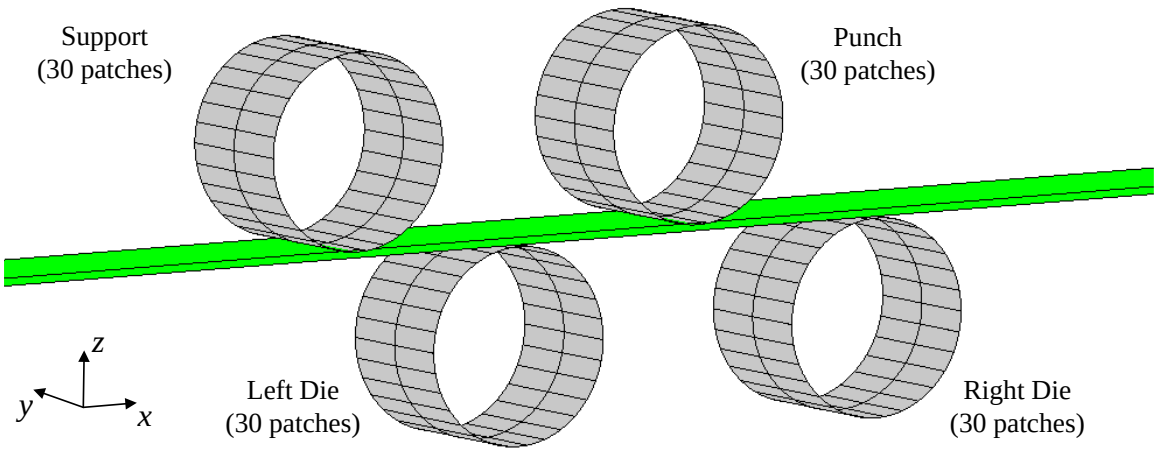

Figure 2.5. Discretization of the tools using Nagata patches.

2.2.3. Process conditions

Considering the sheet flow that occurs in the draw bead test, it is important to discuss both the vertical displacement of the punch (penetration) and the horizontal displacement of the grip. The first stage consists in the vertical movement of the punch in order to create a penetration, p, over the dies (see Figure 2.1). The full punch penetration p_f occurs when $p=2R+t_0$, where R is the radius of the tools and t_0 is the blank initial thickness. When the punch penetration is achieved, the grip displacement is imposed in the horizontal direction, until a fixed value of 150 mm. In this study, the grip conditions are numerically defined using three boundary conditions applied to the third zone of the blank (see Figure 2.4). Two of them constraint the nodes displacements in the thickness direction in two parallel planes, namely $x=411$ mm and $x=450$ mm, which represent the beginning and end of the grip, respectively. The last boundary condition imposes the horizontal displacement of the grip by assigning the nodal displacement in the length direction (150 mm) and it is applied to all nodes in the plane $x=450$ mm. The final stage of the process consists in the removal of the tools, allowing the springback of the blank. Figure 2.6 presents a representative scheme of the draw bead test apparatus as well as the experimental setup.

Regarding the side clearance (or gap), g, between the punch and the dies, it is considered that its value is a multiple of the blank initial thickness. The reference value corresponds to 1.5 times the initial thickness, $g=1.5\ t_0$. The influence of this process parameter will be discussed in detail in Section 4.3.

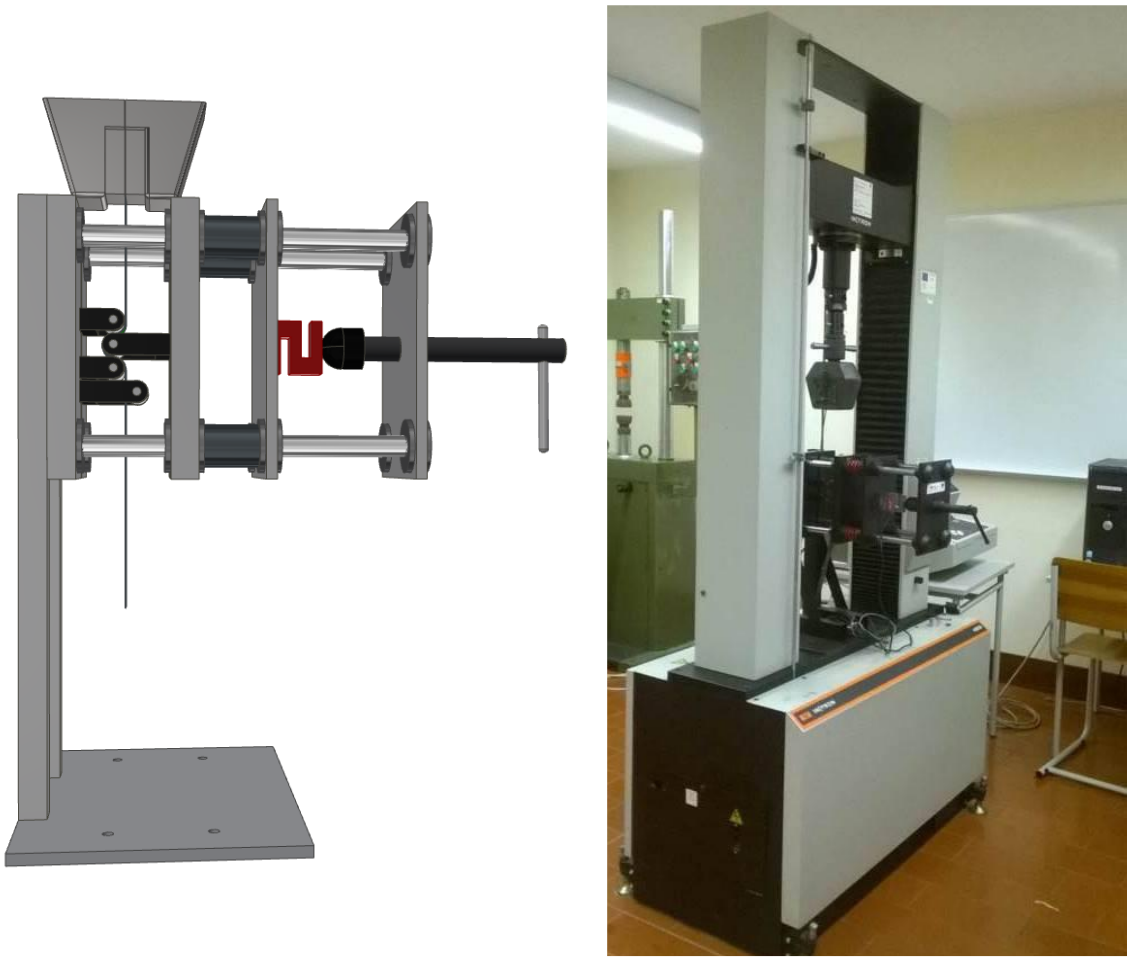

(a) (b)

Figure 2.6. Setup of the draw bead test: (a) Representative scheme; (b) Experimental configuration.

3. Thermal problem analysis

This section contains a brief presentation of the transient thermal problem definition and the finite element formulation. The draw bead test analysis takes into account the heat generated by plastic deformation and friction, as well as the cooling of the blank induced by convection and contact conductance with the tools. Therefore, the heat transfer problem between a heat conductor (blank) and isothermal tools is considered. The analysis present in this section is predominantly focused on the interfacial heat transfer coefficient, which presents a strong impact on the heat transfer between the blank and the tools. Two simple examples are presented in order to study the influence of thermal parameters, namely the ones dictating the heat losses.

3.1. Heat transfer

The differential equation that drives the thermal conduction within a solid body derives from the first principle of thermodynamics coupled with Fourier's heat conduction law, and assumes the following form:

$$\rho c \frac{\partial T}{\partial t} - \mathrm{div}[\mathbf{k} \cdot \mathrm{grad}(T)] - \dot{w}^{\mathrm{p}} - q = 0 \,, \tag{3.1}$$

where ρ is the mass density, c is the specific heat capacity, $\mathbf{k}$ is the thermal conductivity vector, $\dot{w}^{\mathrm{p}}$ is the thermal power associated with the plastic deformation and q is the internal heat generation per unit volume. Regarding the problem under analysis, the factors that enforce the internal heat generation are the occurrence of plastic deformation of the blank and the frictional contact with the tools. The $\dot{w}^{\mathrm{p}}$ term corresponds to the fraction of the plastic power that is converted into heat, and is expressed as:

$$\dot{w}^{\mathrm{p}} = \chi \boldsymbol{\sigma} : \mathbf{D}^{\mathrm{p}} \,, \tag{3.2}$$

where χ is the Taylor-Quinney factor (Taylor and Quinney, 1934), $\boldsymbol{\sigma}$ is the Cauchy stress tensor and $\mathbf{D}^{\mathrm{p}}$ is the plastic strain rate. The heat flux due to the frictional heat generation at the interface is a component of q and can be expressed as:

$$q_{\text{frict}} = \eta\left(\xi\,\mathbf{t}_{\text{t}}\cdot\dot{\mathbf{g}}_{\text{t}}\right), \text{ at } \gamma_{\text{c}}, \tag{3.3}$$

where ξ represents the fraction of generated energy converted into heat, which is partitioned between the solid body and the isothermal obstacle, the parameter η defines the total amount of heat dissipated to the solid body, $\mathbf{t}_{\text{t}}$ is the friction force and $\dot{\mathbf{g}}_{\text{t}}$ is the tangential slip velocity.

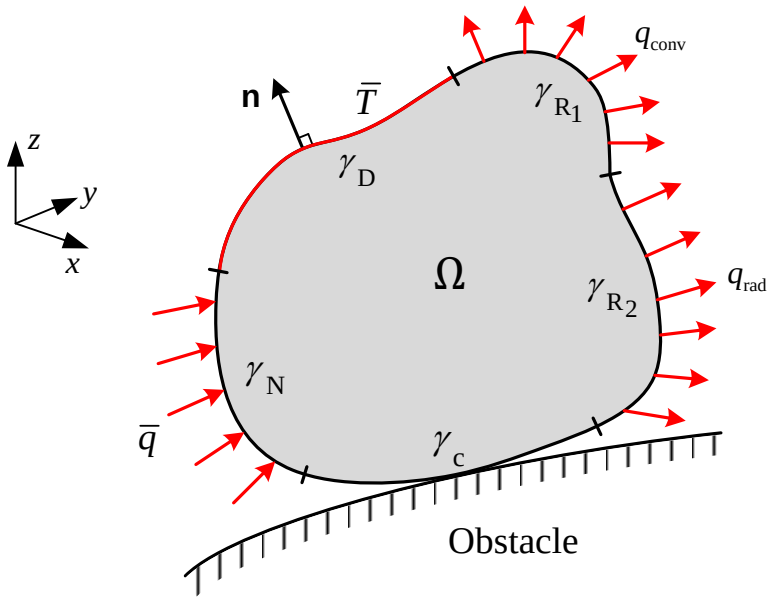

Figure 3.1. Heat conductor solid body in contact with an isothermal obstacle with arbitrary shape and respective boundary conditions.

The transient heat conduction phenomenon is expressed by Equation (3.1), which involves a temperature field dependent on the time. Consequently, it is necessary to know an initial condition for the temperature field, defined as T_0 for the open set Ω in the initial configuration. The remaining boundary conditions are defined on the boundary surface γ, which denotes the limits of the open set Ω (see Figure 3.1). The boundary surface is composed by five sets: $\gamma = \gamma_{\text{c}} \cup \gamma_{\text{D}} \cup \gamma_{\text{N}} \cup \gamma_{\text{R}_1} \cup \gamma_{\text{R}_2}$, that correspond to thermal contact, Dirichlet, Neumann and Robin boundary conditions, respectively. Dirichlet conditions denote an imposed temperature on the surface, while Neumann, Robin and thermal contact conditions impose heat fluxes. These conditions are described by (Teixeira-Dias et al., 2010):

$$T = \bar{T}, \text{ at } \gamma_{\text{D}}, \tag{3.4}$$

$$-\bar{q} = [-\mathbf{k} \cdot \text{grad(T)}] \cdot \mathbf{n} \text{, at } \gamma_N, \tag{3.5}$$

$$q_{conv} = [-\mathbf{k} \cdot \text{grad(T)}] \cdot \mathbf{n} = h_{conv}(T - T_\infty) \text{, at } \gamma_{R_1}, \tag{3.6}$$

$$q_{rad} = [-\mathbf{k} \cdot \text{grad(T)}] \cdot \mathbf{n} = h_{rad}(T - T_r) \text{, at } \gamma_{R_2}, \tag{3.7}$$

$$q_c = [-\mathbf{k} \cdot \text{grad(T)}] \cdot \mathbf{n} = h_c(T - T_{obs}) \text{, at } \gamma_c, \tag{3.8}$$

where **n** is the outward normal vector to the boundary surface, T_∞, T_r and T_{obs} are the environment, radiation surface and isothermal obstacle temperatures, h_{conv}, h_{rad} and h_c are the convection coefficient, radiation coefficient and interfacial heat transfer coefficient (IHTC), respectively. Regarding the radiation coefficient, h_{rad}, it can be defined as:

$$h_{rad} = \kappa_r (T'^2 + T_r'^2)(T' + T_r') , \tag{3.9}$$

where T' and T_r' are the absolute temperatures of the surface γ_{R_2} and the radiation surface, respectively. The parameter κ_r is defined considering the Stefan-Boltzman constant, emissivity of the body and the view factors. The definition of the IHTC will be further discussed in Section 3.1.2.

Applying the principle of virtual temperatures, Equation (3.1) can be discretized as (Martins et al., 2017):

$$\int_\Omega \delta T \rho c \dot{T} \, d\Omega + \int_\Omega \text{grad}(\delta T) \cdot [\mathbf{k} \cdot \text{grad}(T)] d\Omega = \int_\Omega \delta T \dot{w}^p \, d\Omega + \int_{\gamma_N} \delta T \bar{q} \, d\gamma , \tag{3.10}$$

which, in matrix form, is given by:

$$\mathbf{C}\dot{\mathbf{T}} + \mathbf{K}\mathbf{T} = \mathbf{Q} + \mathbf{f} , \tag{3.11}$$

where **C** is the capacity matrix and **K** is the conductivity matrix. **Q** is the vector of nodal heat flux input. Finally, the vector **f** represents the prescribed flows and the boundary terms resulting from the environment and the contact with the arbitrary obstacle.

The integration of Equation (3.11) over time can be performed using the generalized trapezoidal method, which is a one-time step method given by:

$$\mathbf{T}_{t+\Delta t} = \mathbf{T}_t + [\Lambda \dot{\mathbf{T}}_{t+\Delta t} + (1 - \Lambda)\dot{\mathbf{T}}_t]\Delta t . \tag{3.12}$$

This expression represents the temporal discretization of the transient heat conduction equation, where t is the time instant under analysis and Δt the time increment. The parameter Λ varies between 0 and 1, and depending on its value, Equation (3.12) takes the form of different integration methods, as shown in Table 3.3 (Andrade-Campos, 2005).

The algorithm currently implemented in the finite element code DD3IMP considers the fully implicit time integration method ($\Lambda=1$) for the correction step, which is also known as Euler backward method (P. Martins et al., 2016).

Table 3.1. Integration methods and corresponding Λ values.

Time integration method	Λ
Fully explicit	0
Semi-implicit (Crank-Nicolson)	$1/2$
Semi-implicit (Galerkin)	$2/3$
Fully implicit	1

3.1.1. Convective cooling

Since the draw bead test is carried out in an uncontrolled environment (blank and tools in air at ambient temperature), the convective cooling of the blank is an important factor for the thermal analysis. Typically, the heat transfer between the blank and the environment is calculated using Equation (3.6), where the heat transfer coefficient (HTC) presents a vital role, affecting the accuracy of the predicted thermal behaviour due to the heat exchange. Table 3.2 presents the air properties and parameters that will be considered in this section (Bergman et al., 2011)[2].

Table 3.2. Air properties and parameters of the problem.

Property	Value
Blank surface temperature, T_s	308 K
Environment temperature, T_∞	298 K
Average temperature, T_f	303 K
Volumetric thermal expansion coefficient, β	3.3×10^{-3} K^{-1}
Prandtl number, Pr	0.707
Thermal diffusivity, α	2.29×10^{-5} m^2/s
Kinematic viscosity, ν	1.62×10^{-5} m^2/s
Thermal conductivity, k	2.65×10^{-2} W/m·K
Average length of the heat transfer area, L	259.5×10^{-3} m

[2] Air properties were calculated at an average temperature between the blank and the environment. Since the surface temperature is non-uniform and unknown *a priori*, the temperature of the blank surface is assumed 10 K higher than the environment temperature.

Due to the experimental set-up of the draw bead test (see Figure 2.6), it is assumed that the heat transfer occurs by free convection on a vertical plate. Considering a maximum velocity allowed for the grip of 20 mm/s, laminar flow conditions can be assumed. Thus, the average HTC is given by (Bergman et al., 2011):

$$\bar{h} = \frac{\overline{Nu}_L \cdot k}{L}, \tag{3.13}$$

where $\overline{Nu}_L$ is the average Nusselt number, k is the thermal conductivity and L represents the average length of heat transfer area, i.e. the average length of the blank in contact with the air, which changes over the time. For the set-up conditions assumed for the draw bead test, the initial value is 169.5 mm while the final one is 319.5 mm, leading to an average value of 259.5 mm. The Nusselt number is a dimensionless parameter that provides a measure of the convection heat transfer occurring on the surface. For laminar free convection on vertical surfaces is given by:

$$\overline{Nu}_L = 0.68 + \frac{0.670 Ra_L^{1/4}}{[1+(0.492/Pr)^{9/16}]^{4/9}}, \tag{3.14}$$

where Ra_L is the Rayleigh number and Pr is the Prandtl number. The Rayleigh number is the product of the Grashof and Prandtl numbers, which for laminar vertical plates is given by:

$$Ra_L = \frac{g_a \beta (T_s - T_\infty) L^3}{\alpha \nu}, \tag{3.15}$$

where g_a is the gravitational acceleration, β is the volumetric thermal expansion coefficient, T_s is the blank surface temperature, T_∞ is the environment temperature, α is the thermal diffusivity, L is the average length of heat transfer area and ν is the kinematic viscosity.

Substituting the values presented in Table 3.2 in Equation (3.15), the value of the Rayleigh number obtained is 1.5×10^7, which is inferior to the transition to turbulent regime value of 10^9, confirming laminar flow conditions. Then, substituting the Rayleigh and Prandtl numbers in Equation (3.14) the average Nusselt number obtained is 32.7. Finally resolving Equation (3.13), the obtained value for the HTC is 3.4 W/m^2 K. The small value can be explained by the reduced temperature gradient and lack of forced flow on the surface.

3.1.2. Thermal contact conductance

Despite the loss of heat to the environment through natural convection, the contact between the blank and the tools leads to an important heat loss, which must be considered. The main parameter that controls the thermal contact conductance is called interfacial heat transfer coefficient (IHTC). Considering the contact between the blank and the tools, the IHTC acts as a global heat transfer coefficient. Its value can be obtained through an equivalent thermal circuit where the only thermal resistance is the contact resistance. Although theories have been developed for predicting the contact resistance, the most reliable results are those that have been obtained experimentally (Bergman et al., 2011). The thermal contact resistance relates to the IHTC through:

$$U = \frac{1}{R_t''}, \tag{3.16}$$

where U is the global heat transfer coefficient and R_t'' is the contact resistance. The thermal contact resistance depends greatly on the contact pressure. Accordingly, taking into account the values of contact pressure arising in the draw bead test, as well as the typical values present in sheet metal forming (Chang et al., 2016; Pereira et al., 2008), the value of 10 MPa contact pressure was selected (higher value in (Bergman et al., 2011)). For this value of contact pressure, the contact resistance ranges from 0.7×10^{-4} m^2·K/W to 4.0×10^{-4} m^2·K/W. Thus, three values of R_t'' for metallic interfaces were selected to evaluate the influence of the IHTC on the predicted temperature (Bergman et al., 2011), which are listed in Table 3.3.

Table 3.3. Relationship between the thermal contact resistance and the corresponding IHTC value for 10 MPa of contact pressure between metallic interfaces (Bergman et al., 2011).

R_t'' [m^2·K/W]	IHTC [W/m^2·K]
2.7×10^{-4}	3700
3.2×10^{-4}	3100
4.0×10^{-4}	2500

Regarding the behaviour of the IHTC in the area near the contact with the tools, some adjustments must be made in order to properly describe the variation from the IHTC value to the HTC value that describes the heat transfer with the environment. In this work the

IHTC is considered as only being dependent on the gap distance, g_n, between the blank and the tools, and its numerical variation is described as follows (P. Martins et al., 2016):

$$h_{int}(g_n) = h_{sup} \exp(m\, g_n), \tag{3.17}$$

where h_{int} is the evolving IHTC, being h_{sup} the upper IHTC threshold value and m a parameter that controls the rate of increase/decrease of the IHTC, which is adjusted so that h_{int} matches the HTC value when g_n reaches 1 mm. This law for the IHTC permits a smooth transition from the heat transfer coefficient value verified in the contact area to the one observed for the environment. Figure 3.2 shows the variation of the IHTC in the proximities of the contact zone, as a function of g_n. It is assumed that for distances higher than 1 mm of gap, the value of h_{int} tends to the HTC calculated in Section 3.1.1. The m values determined for each IHTC presented in Table 3.3 are 7.01, 6.83 and 6.61, for decreasing IHTC values.

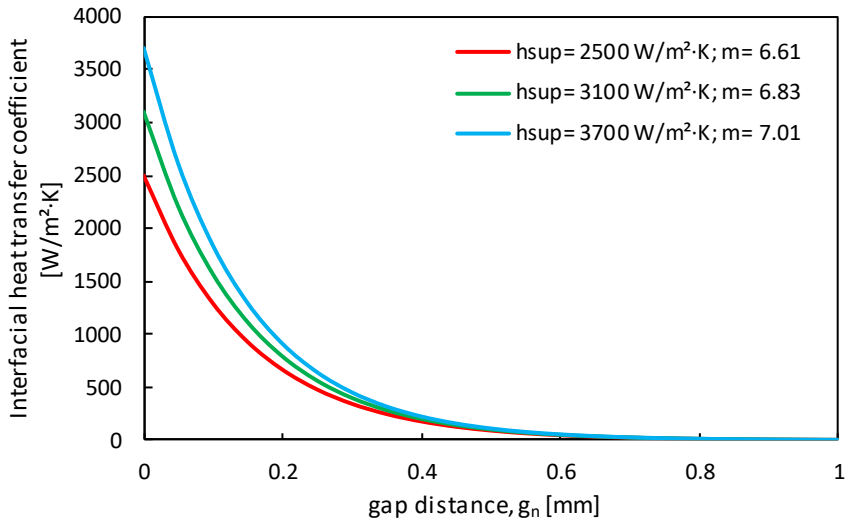

Figure 3.2. Distribution of the h_{int} value in the transition zone between contact and non-contact (convective cooling) for the three different values of assumed for the IHTC.

3.2. Strip drawing test (flat tools)

The first example consists of a blank clamped between two parallel flat tools. The blank is subsequently pulled in order to produce relative movement between the bodies and, consequently, friction forces. The heat transfer coefficient h_{int} is assumed constant in all exterior surface of the blank, i.e. identical for both contact tool-metal (IHTC) and environment-metal (HTC). The purpose of this example is to evaluate the influence of the h_{int} in the predicted temperature under frictional conditions (μ=0.15), excluding heat

generation by plastic deformation. For this example, three values for the h_{int} were chosen to evaluate the predicted temperature. The lower value corresponds to 1 $W/m^2 \cdot K$, which tries to replicate thermal isolation conditions, meaning that the heat exchanges with the exterior are negligible. The second value is 100 $W/m^2 \cdot K$ and the third is 1000 $W/m^2 \cdot K$. It is assumed a constant pulling velocity of 1 mm/s.

3.2.1. Finite element model

The presented example considers a deformable body (sheet) in contact with two rigid surfaces (flat tools). Due to material and geometrical symmetry conditions, only half sheet width is considered. The blank discretization is divided in two zones along the *x*-direction. The first zone of the blank will be in contact with the tools (finite element size of 0.26 mm) and the second zone represents the contact with the grip, having only one FE for the whole contact in the length direction. In the width direction 10 finite elements are considered, while 3 finite elements are considered in the thickness direction. The entire blank comprises 4,530 finite elements. Figure 3.3 shows the geometrical conditions adopted, as well as the blank zones described above.

This example is divided in two phases, the first consists in the movement of the upper and lower tools to compress the blank (without inducing plastic strain). The second phase consists in pulling the blank in the *x*-direction for 80 mm, to generate heat through frictional contact with the tools. The two flat tools are both modelled with Nagata patches. In this case, as they are flat, only one patch was considered for each tool. The elastic properties considered are the ones presented in Section 2.2.1.

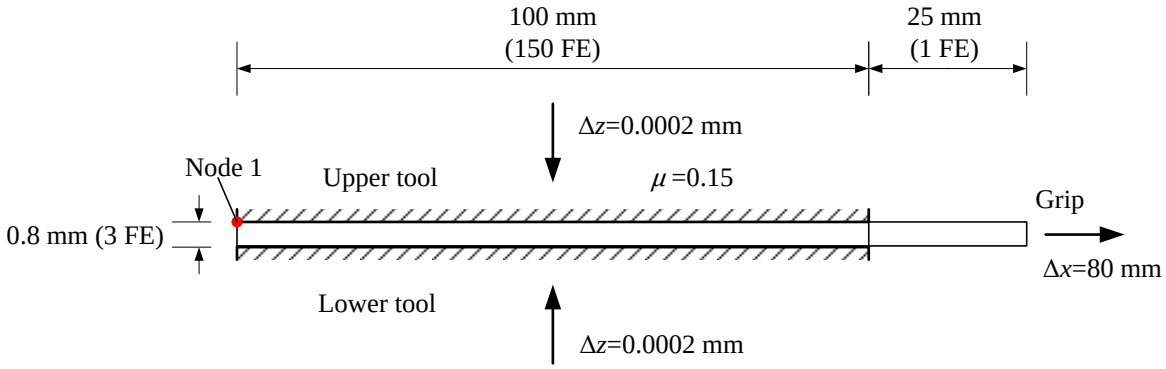

Figure 3.3. Representative scheme of the example with flat tools.

3.2.2. Results and discussion

As expected, in the case of h_{int} equal to 1 W/m^2·K (very low value), the blank temperature increases gradually during the entire pulling displacement. This shows that the heat lost to the tools and the environment is very low (see Figure 3.4). For the intermedium value of h_{int}, the predicted temperature reaches a steady state regime near 40 mm of pull displacement (temperature variation of about 32 K). This denotes a slower temperature variation than in the first case, explained by the higher heat exchanges at the boundaries of the blank (see Figure 3.4). Finally, for the higher value of the HTC, the predicted temperature remains almost unchanged throughout the whole pulling displacement, meaning that all the generated heat is lost to the tools and the environment. Figure 3.4 shows the temperature variation for the three tested h_{int} values.

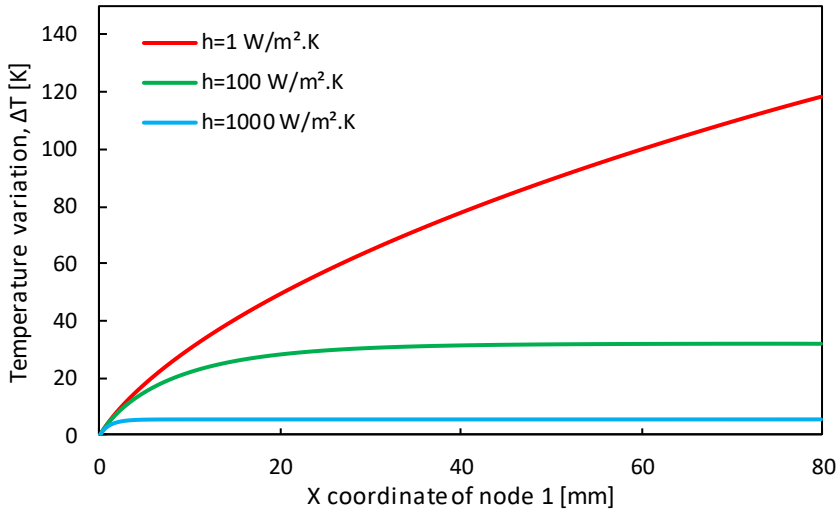

Figure 3.4. Temperature variation evaluated for node 1, for different h_{int} values.

The main conclusions achieved with this first example are that for higher h_{int} values, the predicted temperature reaches a steady state regime sooner. Moreover, the increase of the heat transfer coefficient promotes more heat exchanges with the exterior, causing the predicted temperature to decrease, as more energy is released. Notice that in the three cases the energy generated by friction is the same.

However, the assumption of equal heat transfer coefficients in the contact between tool-sheet and environment-sheet is not valid, because contact conditions are

different in both cases. Therefore, in the second example different values will be taken into account, to correctly predict the temperature in both contact conditions.

3.3. Strip drawing test (rounded tools)

The second example considers the deformable body used in the first example, but now in contact with two rigid rounded surfaces (rounded tools). The boundary conditions are the same as in the first example. In this case, it is considered that the heat transfer occurs differently in the contact area with the tools and the environment. Thus, two values of heat transfer coefficient will be used, one for the contact environment-sheet (HTC) and one for the contact tool-sheet (IHTC). The adopted value for the HTC is 3.4 $W/m^2 \cdot K$ (see Section 3.1.1) and for the IHTC three values were chosen (see Section 3.1.2).

The same process conditions of the first example were adopted, to generate heat through frictional contact with the tools, but in this case with different heat transfer coefficients. The main difference from the first example is in the geometry of the tools, which in this case promotes heat transfer not only in the contact area, but also in the proximities of the contact, where the heat transfer coefficient is evaluated based on Equation (3.17). Furthermore, in this example the influence of the pulling speed in the predicted temperature will be studied.

The blank is the same deformable body of the first example, including the discretization. The two rounded surfaces (rounded tools) with plane contact area are modelled with 34 Nagata patches. The boundary conditions used are the same of the first example.

This example is also divided in two phases, where the first consists in the movement of the upper and lower tools to compress the blank (without inducing plastic strain) and the second phase consists in pulling the blank in x-direction for 80 mm, to generate heat through frictional contact with the tools (μ=0.15). The initial value of the puling speed is 1 mm/s.

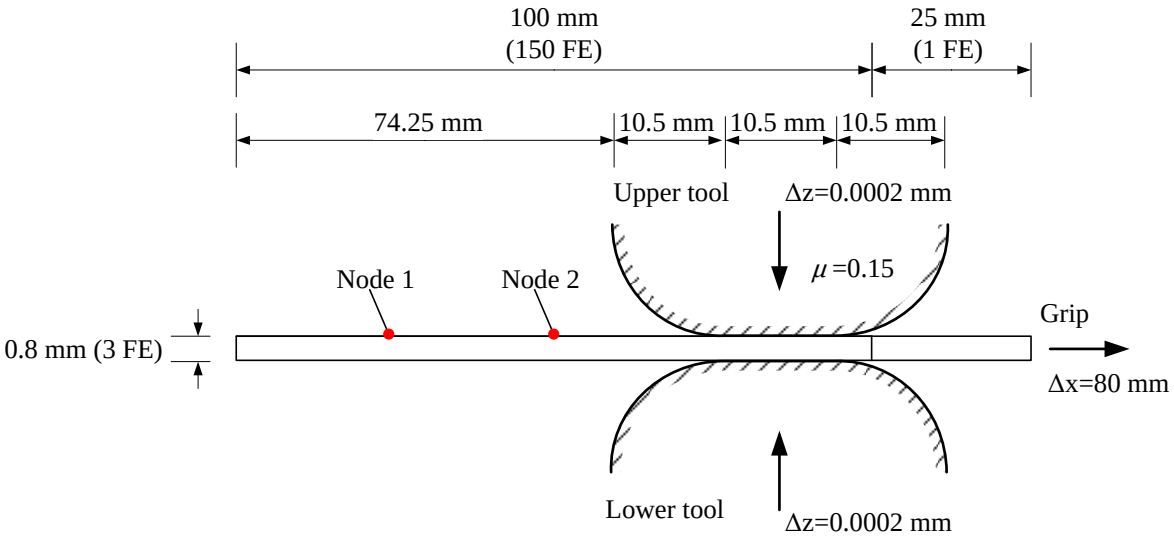

Figure 3.5. Representative scheme of the example with rounded tools.

3.3.1. Results and discussion

The distribution of the h_{int} as a function of the gap distance to the tools is presented in Figure 3.2, considering three distinct maximum values. Its influence on the temperature distribution is presented in Figure 3.6. Since the temperature on the sheet is non-uniform, two nodes of the finite element mesh were selected to evaluate the temperature evolution.

Although the selected nodes have different positions, both reach the peak of temperature in the same position, which corresponds to the contact area with the tools (see Figure 3.5). Considering different IHTC values, the evolution of the temperature is similar, ranging in a small interval (1 K of temperature variation for the three different IHTC values). Nevertheless, it should be noted that the maximum temperature variation is about 3 K, which occurs when the minimum value of IHTC is adopted. In fact, the temperature variation increases approximately 50% when the IHTC decreases from 3700 to 2500, as highlighted in Figure 3.6. Nevertheless, it should be mentioned that this temperature variation is much smaller than the observed in Figure 3.4.

Since the initial position of node 2 is closer to the tools (contact region), the temperature increase rate is higher in this node, due to the proximity with the heat source and the thermal conduction (see Figure 3.6). Once node 1 becomes closer to the contact area, is has almost the same behaviour as node 2, reaching the same temperature gradient in the

same spatial position (under the tools). After losing contact with the tools, the temperature of the sheet decreases and then stabilizes (low gradient) when the IHTC assumes the HTC value (3.4 $W/m^2 \cdot K$).

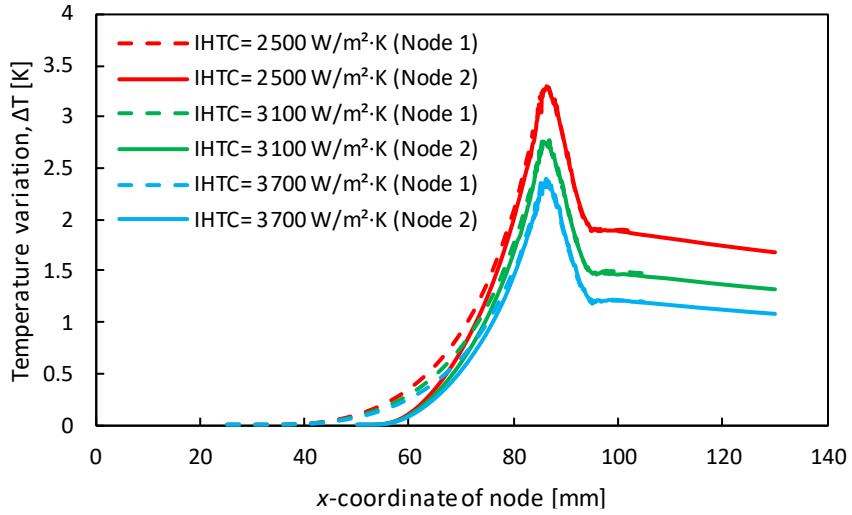

Figure 3.6. Temperature distribution for different IHTC values of node 1 and node 2.

In order to study the impact of the sliding velocity on the predicted temperature, three velocity values were chosen. Nevertheless, the thermal conditions that establish the heat transfer between the sheet and the tools and environment are assumed constant, i.e. the HTC and IHTC values are 3.4 $W/m^2 \cdot K$ and 3100 $W/m^2 \cdot K$, respectively. The selected values for the grip velocity are 1 mm/s, which was already studied, 5 mm/s and 10 mm/s.

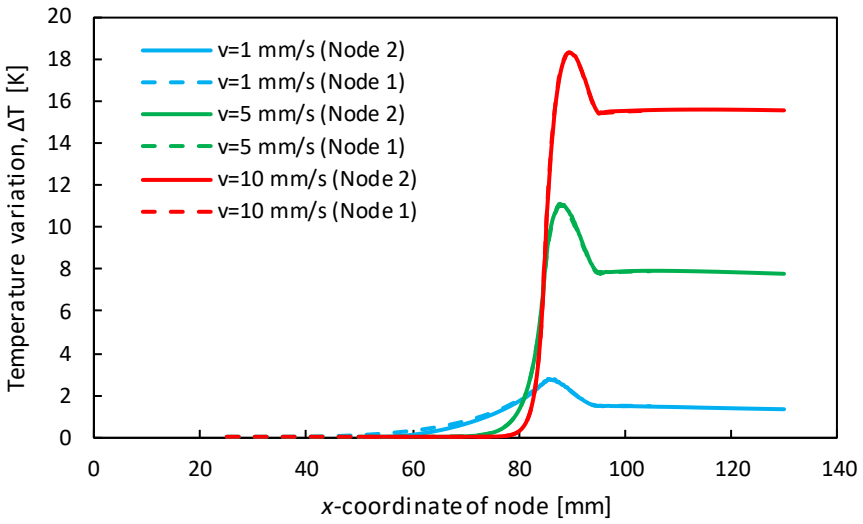

Figure 3.7. Temperature distribution in nodes 1 and 2 for different pulling speeds.

Figure 3.7 shows the temperature variation for the different conditions. The increase of the pulling velocity results in a higher temperature, due to the higher slip rate (see Equation (3.3)). The maximum temperature variation attained is approximately 18 K, occurring for the 10 mm/s of pulling speed (see Figure 3.7). The different behaviour of node 1 and node 2 verified in Figure 3.6 tends to disappear for higher velocities, i.e. the temperature evolution of the node 1 is identical to the one of node 2. This results from the speed up of the heating process which reduces the contribution of the conduction within the blank, resulting in the slow increase of the blank temperature. The peak of the temperature continues to be in the same *x*-coordinate, corresponding to the contact between the blank and the tools.

The main conclusions from the variation of the pulling velocity are that the predicted temperature increases with the increase of the velocity and that the heat conduction process becomes negligible for higher velocities.

4. Thermomechanical results and discussion

This section presents the numerical simulations results of the draw bead test, comparing several sets of process conditions. All simulations are performed considering the DP780 blank material, except where indicated. The variables under analysis are the contact forces, the strain, the temperature, the contact angles and the springback. These variables are evaluated for different process conditions, such as punch penetration, side clearance and friction coefficient. This analysis is performed considering always as reference the model with: (i) 21.8 mm of punch displacement (p_f); (ii) 150 mm of grip displacement; (iii) 1 mm/s of pulling speed; (iv) side clearance of 1.2 mm (1.5 t_0) and (v) friction coefficient of 0.15. First, in order to reduce the computational cost, the adoption of plane strain conditions is explored (2D model) to describe the draw bead test. Then, the influence of the process parameters and the selected material (DP500 and DP780) with regards to the variables mentioned previously is analysed.

4.1. Plane strain conditions

In order to assess the influence of the assumption of plane strain conditions, both 2D and 3D models, described in Section 2.2.2, were analysed. The comparison between the finite element models considers the main process parameters, which are the contact forces and angles and temperature evolution that occurs in the draw bead test.

Regarding the contact forces arising in the draw bead test, the most influent ones are the punch force and the grip force. The comparison between the 2D and 3D models regarding the forces is presented in Figure 4.1 and Figure 4.2. The behaviour of the forces – punch force in the *z*-direction, P_z, during punch displacement and grip force in the *x*-direction, G_x, during grip displacement – is identical for the 2D and 3D models. Thus, the adoption of plane strain conditions does not affect the predicted forces in the test. Further attention will be given to these forces in Sections 4.2 to 4.5.

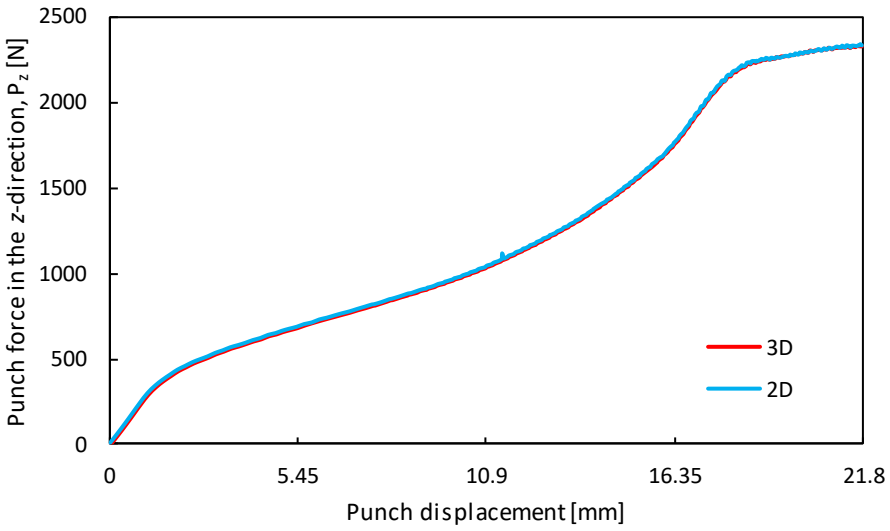

Figure 4.1. Punch force in the *z*-direction, P_z, during the punch displacement. Comparison between 2D and 3D models.

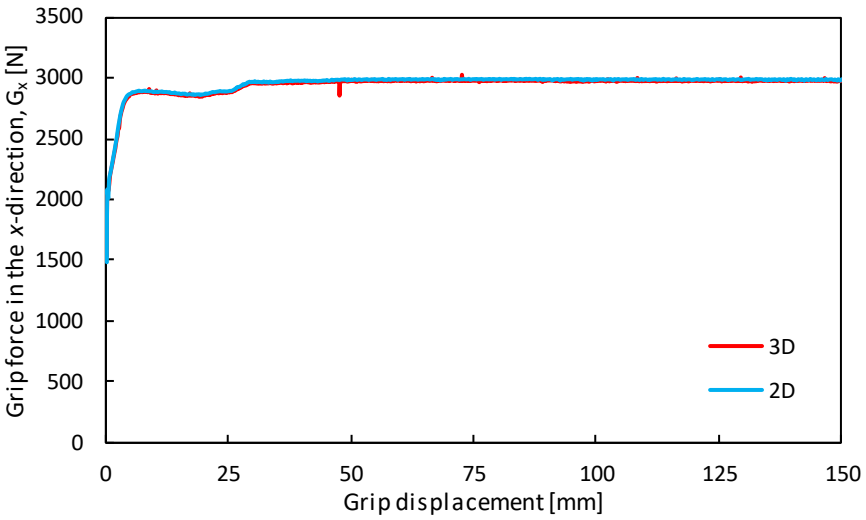

Figure 4.2. Grip force in the *x*-direction, G_x, during the grip displacement. Comparison between 2D and the 3D models.

The contact angle between the blank and the tools (cylinders), excluding the support cylinder, is evaluated for both models. Hence, three contact angles are considered, θ_1, θ_2 and θ_3, which describe the contact with the left die, punch and right die, respectively. These angles were obtained by considering the first and last node of the blank in contact with each tool. Figure 4.3 shows the adopted angle definition, as well as the location of the contact forces (explanatory case). These three angles were evaluated for eight instants of the test, four during the displacement of the punch and the remaining four during the grip

displacement. The selected instants correspond to equidistant values of displacement, i.e. 5.45 mm of punch displacement and 37.5 of grip displacement.

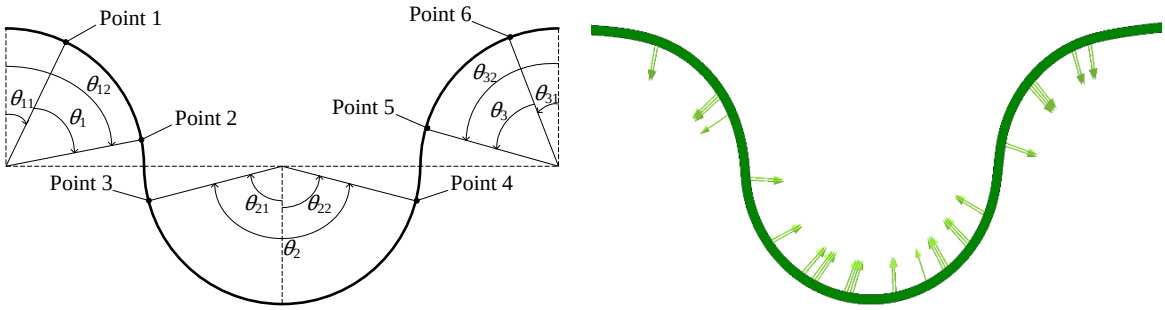

Figure 4.3. Contact angles definition: (a) schematic approach; (b) location of the contact forces in the draw bead (end of phase 1).

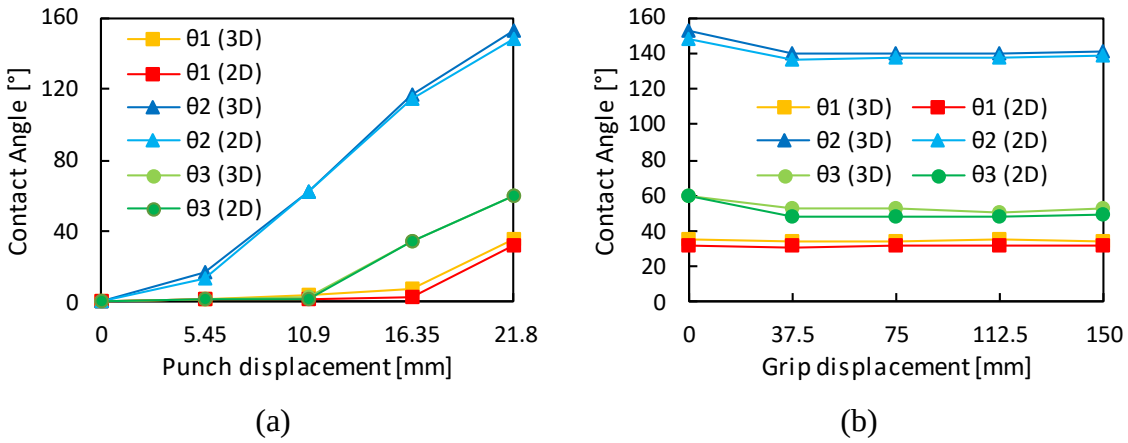

Figure 4.4. Evolution of the contact angles θ_1, θ_2 and θ_3: (a) during the punch displacement; (b) during the grip displacement.

Figure 4.4 presents the contact angles for the 2D and 3D models. The behaviour of the angle differs from the punch displacement to the grip displacement, due to the nature of the movement. The vertical movement of the punch leads to an increase of the angle θ_2 since the beginning, while the angles θ_1 and θ_3 start to increase only when the punch displacement reaches 10.9 mm. For 21.8 mm of vertical displacement (full punch penetration), θ_1, θ_2 and θ_3 reach the maximum values, which are about 34°, 150° and 60°, respectively. During the displacement of the grip the contact angles tend to stabilize at around 37.5 mm, after a slight decrease in relation to its initial values (final values achieved at the end of the vertical displacement of the punch). The values of θ_1, θ_2 and θ_3 remain

stable after 37.5 mm of grip displacement and are approximately 33°, 140° and 50°, respectively.

Comparing the angles predicted by the 2D and the 3D models, the global difference (considering the eight values of the angles for each model) never exceeds 4.6°. This maximum difference occurs for θ_2 when the grip displacement reaches 37.5 mm. The overall average difference between the two models is 2.3°, being the lower angle predicted by the 2D model.

Regarding the springback effect, the comparison is performed considering the angle between the two non-deformed zones of the blank (located before the support cylinder and after the right die). Figure 4.5 shows the springback differences between the 2D and 3D model, as well as a scheme of the springback angle considered.

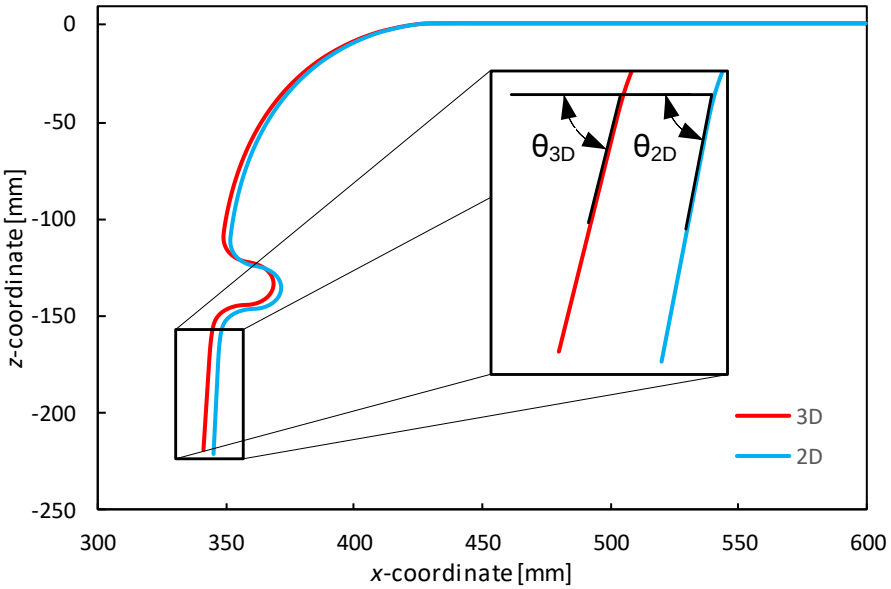

Figure 4.5. Springback of the blank considering the 2D and the 3D models. Detail of the springback angle definition.

The springback angle predicted by the 3D model, θ_{3D}, is 87.2° while for the 2D model is 87.8°. The difference between the springback angles is lower than 1°, which shows a good agreement of both models. Although the springback angle is identical, the final geometry of the 2D model presents some differences, as shown in Figure 4.5.

Since the heat generated by plastic strain and frictional contact is taken into account in the finite element analysis, the temperature of the blank is not uniform. Hence, it

is important to analyse the blank temperature (evolution and distribution at the end), as predicted by the numerical models. Figure 4.6 presents the temperature distribution of the whole blank at the end of the second phase (grip displacement), as well as the equivalent plastic strain. Figure 4.7 shows the evolution of the temperature for a reference node (node 1), which is initially before the tools and throughout the test performs the whole contact with tools and reaches a steady state.

Considering the temperature distribution (Figure 4.6), two planes parallel to the length direction: y=0 mm and y=12.5 mm are used to assess the temperature. The main heat generator factor is the plastic strain rate. Considering the 2D model, the equivalent plastic strain (EPS) is the same in both planes due to the boundary conditions. On the other hand, some deviations in the equivalent plastic strain are predicted by the 3D model (see Figure 4.6) case, when comparing both planes, causing different temperatures. The temperature distribution correlates with the equivalent plastic strain distribution (see Figure 4.6). In the plane y=12.5 mm, the EPS behaviour of the 3D model shows an increase of its maximum value, resulting in the maximum temperature predicted (see Figure 4.6).

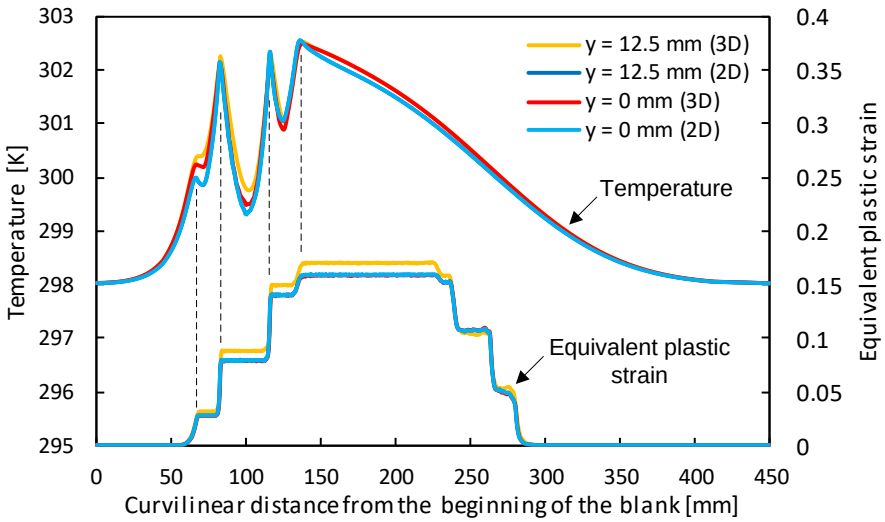

Figure 4.6. Temperature and equivalent plastic strain distributions obtained at the end of the second phase (grip displacement). Comparison between 2D and 3D models.

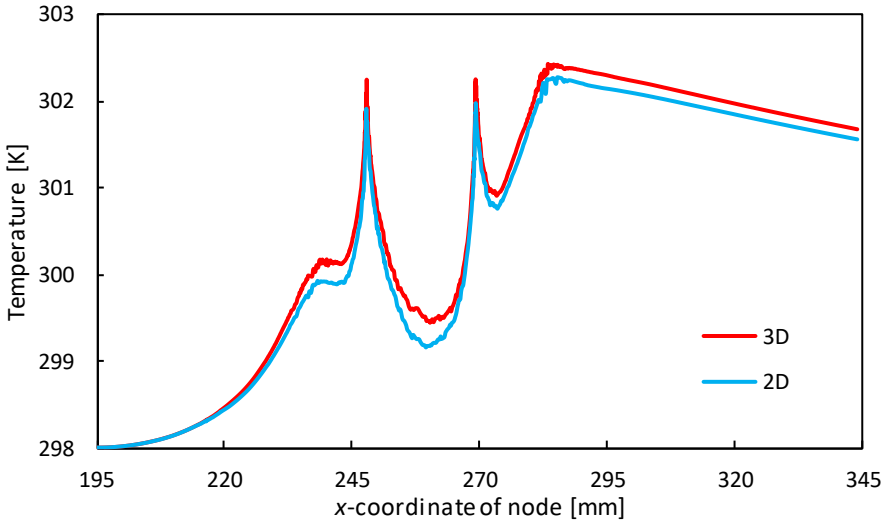

Figure 4.7. Comparison of the temperature evolution in node 1 achieved for the 2D and 3D models.

Since the draw bead test reaches a steady state, the temperature evolution in a node that travels all path defined by the tools is identical to the temperature distribution along the strip (compare Figure 4.6 and Figure 4.7). The behaviour of the temperature evolution is very similar for both models (Figure 4.7). Indeed, the maximum temperature achieved for the reference node in the 2D model is about 302.3 K, while for the 3D model is approximately 302.4 K. It is worth mentioning that there are slight differences in the temperatures between Figure 4.6 and Figure 4.7, since one represents the global temperature and the other represents the temperature verified in a single node.

The model considering plane strain conditions comprises fewer finite elements (FE), i.e. only two in the width direction. This is advantageous for the computational cost, which is greatly reduced in comparison with the 3D model. Table 4.1 presents the number of FE and the computational time required by each model. The 2D model comprises approximately 7.5 times less finite elements than the 3D model. This decrease in the number of FE improves the computational time about 5 times with respect to the 3D model, which constitutes a considerable improvement in the overall simulations times.

Table 4.1. Comparison between 2D and 3D models with respect to computational time and number of FE.

Model	Finite elements	Computational time [hh:mm:ss]
2D	7584	06:19:57
3D	37920	47:19:29

The overall results are qualitatively similar between models, i.e. the 2D model provides accurate enough results in comparison with the 3D model, while the computational cost is strongly reduced (see Table 4.1). Based on the main process variables analysed (forces, temperatures, angles) and the computational performance of each numerical model (2D and 3D), plane strain conditions will be considered in the following sections.

4.2. Punch penetration

In this section, the influence of the punch penetration is studied, i.e. its impact on the predicted forces, temperatures and contact angles that occur in the test is evaluated. It is assumed that the other process conditions, such as side clearance, material properties and pulling velocity are constant. Three numerical simulations were performed, considering 21.8 mm, 16.35 mm and 10.9 mm of punch displacement, representing 1 (p=1 p_f), 0.75 (p=0.75 p_f) and 0.5 (p=0.5 p_f) times the full penetration, p_f, respectively.

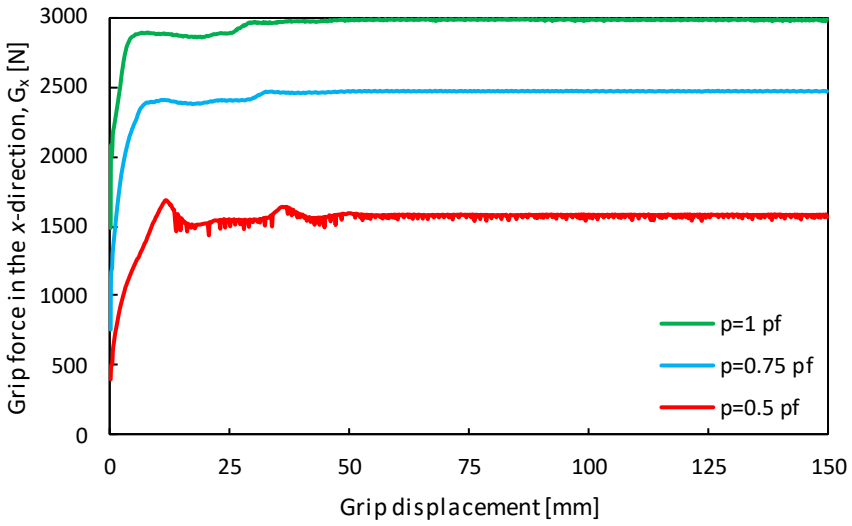

Figure 4.8. Grip force evolution for the three different values of punch penetration.

The evolution of the grip force, G_x as a function of the grip displacement is presented in Figure 4.8, comparing three values of punch penetration. The higher value of grip force occurs for the full penetration, as expected, reaching 2980 N. The difference between the higher and intermediate values of penetration is about 500 N, while for the intermediate and lower cases the difference is about 900 N, as shown in Figure 4.8. The value of grip displacement for which the force attains its steady state decreases when the

punch penetration increases. Nevertheless, for all penetration values, the grip force is approximately constant for a grip displacement higher than 50 mm.

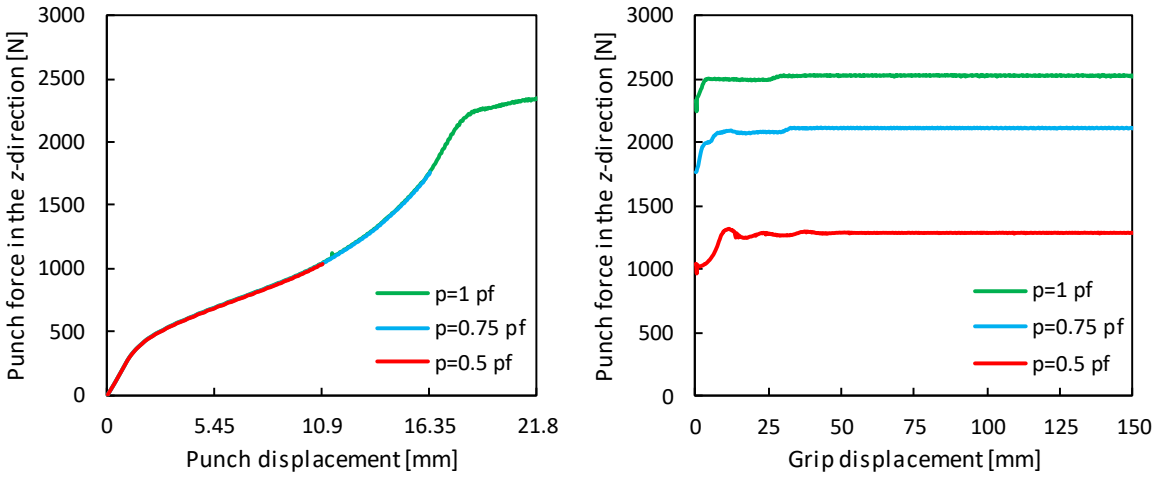

(a) (b)

Figure 4.9. Evolution of the punch force in the *z*-direction, P_z, for the three values of punch penetration: (a) during the punch displacement; (b) during the grip displacement.

The evolution of the punch force in the *z*-direction, P_z, is presented in Figure 4.9 (a) for all penetration cases. Since the difference is only in the displacement for which the penetration ends, the force evolution is the same for all conditions, as expected. The main difference occurs in the maximum values due to the imposed displacements, meaning that the higher forces occur for the higher displacements. The maximum values of P_z are approximately 1043 N for the p=0.5 p_f, 1750 N for the p=0.75 p_f and 2347 N for the p=1 p_f cases.

The evolution of P_z as a function of the grip displacement is presented in Figure 4.9 (b). The higher values of force occur for the higher punch penetrations, reaching the maximum value of approximately 2530 N, for the p=1 p_f case. The punch force reaches a steady state value for a grip displacement higher than 50 mm. This is in accordance with the grip force evolution (see Figure 4.8). In fact, the effect of the punch penetration on the punch force is identical to the one observed in the grip force. Nevertheless, the value of the punch force in the steady state regime is higher than the one observed at the end of punch displacement (Figure 4.9 (a)). Indeed, the punch force increases about 15 % until achieving its constant value.

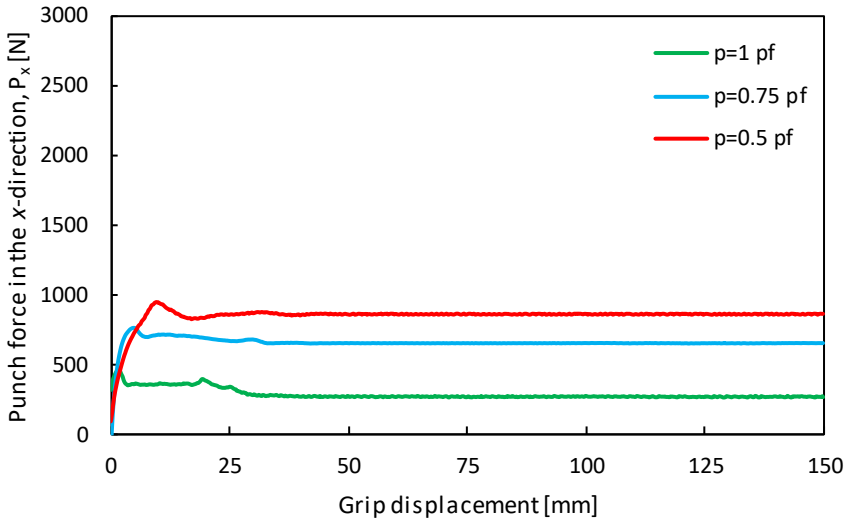

Figure 4.10. Evolution of the punch force in the *x*-direction, P_x, during the grip displacement for the three values of punch penetration.

The evolution of the punch force in the *x*-direction, P_x, with respect to the grip displacement is presented in Figure 4.10, comparing the three values of penetration. In contrast with P_z, which increases with the punch penetration (see Figure 4.9 (b)), P_x decreases as the punch penetration increases. In fact, this switch in the force is due to the blank increasing the contact area with the punch. As shown in Figure 4.3 (a), the angle θ_2 is the sum of θ_{21}, which is the angle of contact of the left side of the punch, and θ_{22} which is the contact angle on the right side of the punch. For the lower penetration case, it is noticeable that there is no contact on the right side of the punch (see Figure 4.11), while for the intermediate and full penetration cases there is contact on the right side of the punch (θ_{22}), creating a force in the opposite direction, decreasing P_x. Thus, the higher P_x value arises for the lower penetration value, reaching approximately 858 N (see Figure 4.10). However, the vertical component of the punch force is always higher than the horizontal component (compare Figure 4.9 (b) with Figure 4.10). The shape of the blank for each penetration value is in agreement with the geometry predicted by (Nine, 1982).

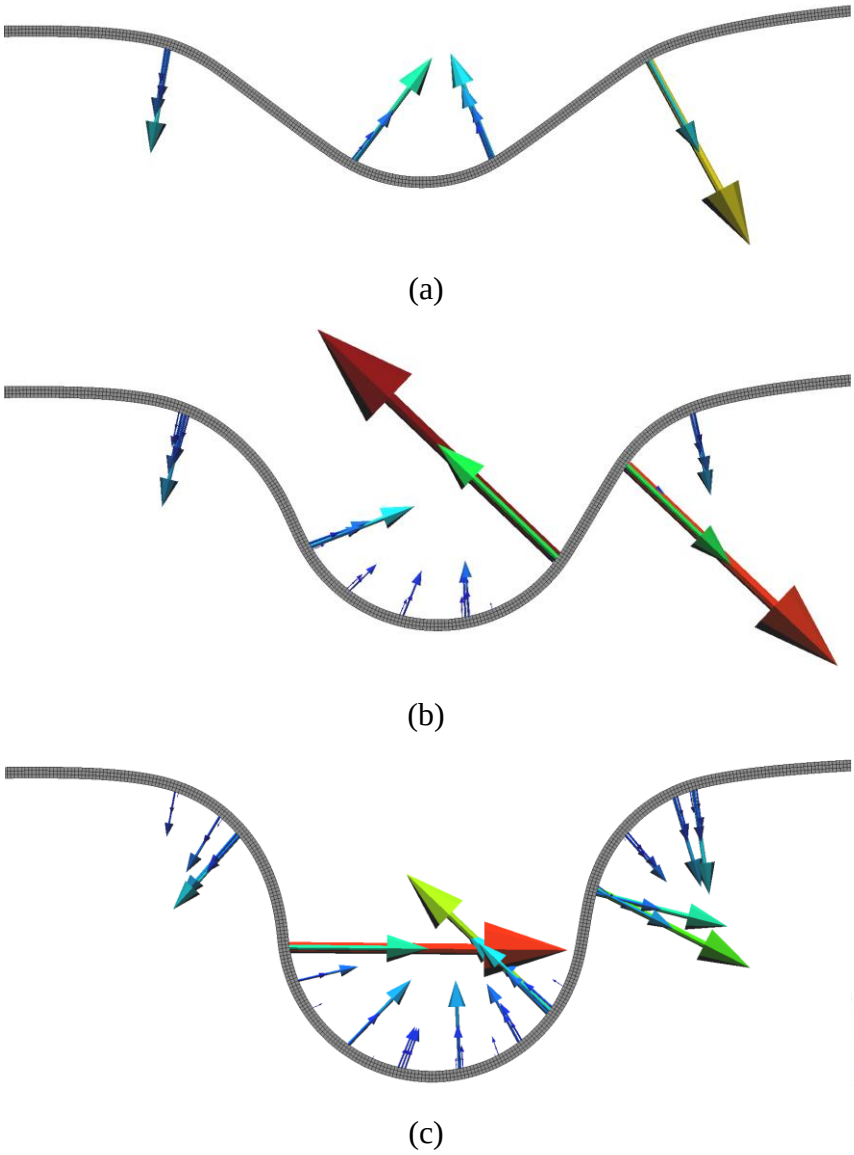

Figure 4.11. Contact forces for three values of punch penetration: (a) p=0.5 p_f; (b) p=0.75 p_f; (c) p=1 p_f. Pulling from left to right.

Regarding the influence of the punch penetration on the contact angles, θ_1, θ_2 and θ_3, the comparison is performed by comparing the angle values observed at a moment where a steady regime is already achieved, i.e. when the grip displacement is comprised between 37.5 mm and 150 mm. Thus, the displacement chosen to evaluate the angles is approximately 112.5 mm. Figure 4.12 presents the contact angles for the three different punch penetrations studied. The higher values of the contact angles arise for full penetration conditions, reaching 31.4°, 137.4° and 48.4° for θ_1, θ_2 and θ_3, respectively. Besides, the angles behave differently depending on the penetration. While θ_2 and θ_3 increase with the

penetration, θ_1 remains almost unchanged (except for full penetration). For the lower punch penetration, the overall contact angles are very reduced, resulting in a contact angle of 32.8° for the whole contact area.

Taking into the contact angles shown in Figure 4.12 for full penetration, the maximum pressure calculated for the steady state regime is about 16.7 MPa, located in the right die (RD). However, as highlighted in Figure 4.11, the contact forces are not continuously distributed in the surfaces, which leads to approximations for the maximum contact pressure of about 150 MPa (also for the RD).

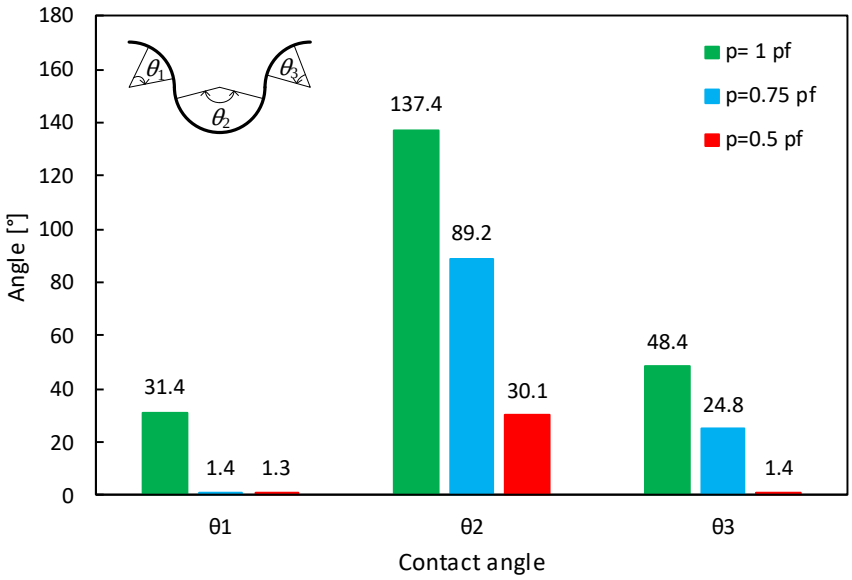

Figure 4.12. Contact angles θ_1, θ_2 and θ_3 achieved for a grip displacement of 112.5 mm. Comparison between p=1 p_f, p=0.75 p_f and p=0.5 p_f.

The temperature and EPS distributions, at the end of pulling stage, are shown in Figure 4.13. The location of the peaks of temperature do not match for the three studied values of punch penetration due to the different contact angles. The maximum temperature occurs for the lower punch penetration value. Although the EPS presents lower values, the temperature reaches the value of 304.6 K due to the reduced contact angle. Although the tools are responsible for generating heat induced by plastic strain, they are also responsible for the main heat loss due to the high thermal contact conductance. Thus, inferior contact angles (Figure 4.12) results in lower heat generation but also inferior heat losses.

The contact angle presents a strong influence on the maximum temperature, as shown in the temperature evolution of node 1, presented in Figure 4.14. Indeed, for full penetration, the maximum temperature is the lowest of the three cases, as it registers the biggest contact angle, despite having the highest EPS value, reaching 302.6 K. Considering the lower penetration value, the reason why the temperature of the node 1 does not present a similar decrease as the others, in the contact zone with the punch (between the first two peaks), is due to the small contact angle θ_2 (30.1°). The same reason applies to the maximum temperature observed (node 1) of 304.3 K.

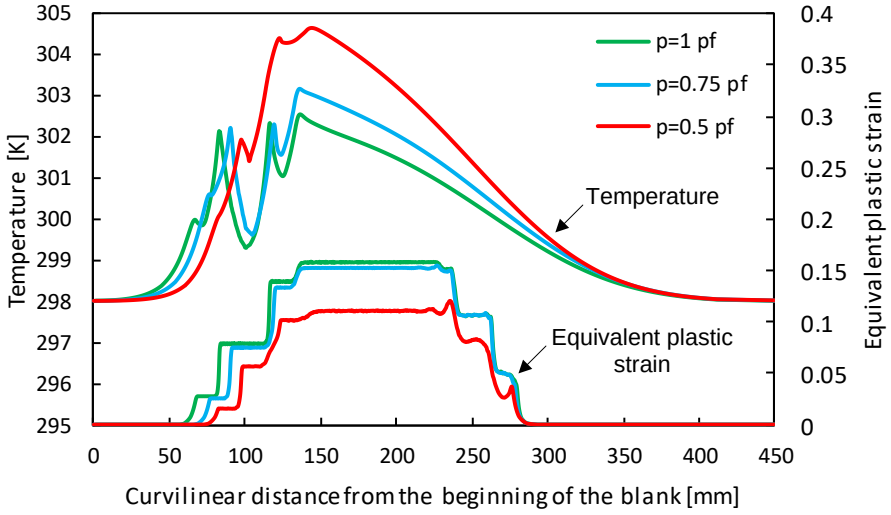

Figure 4.13. Temperature and equivalent plastic strain distributions obtained at the end of the second phase. Comparison between the considered punch displacements: p=1 p_f, p=0.75 p_f and p=0.5 p_f.

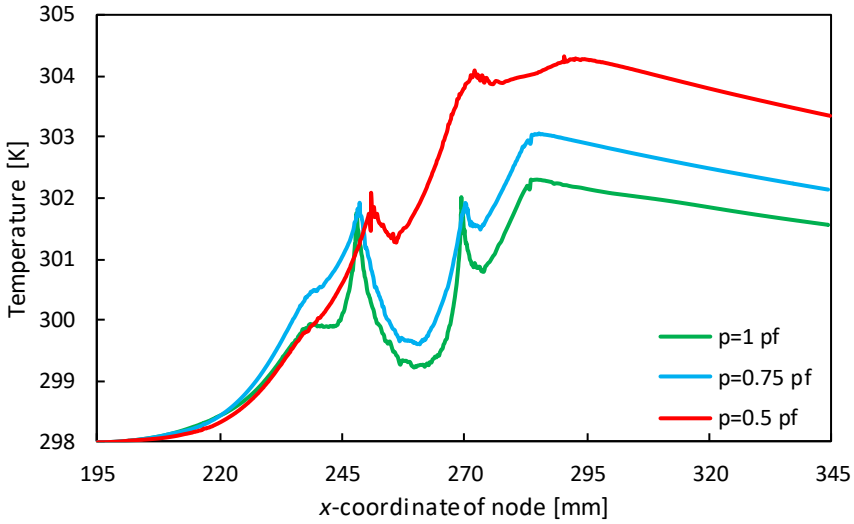

Figure 4.14. Temperature evolution achieved in node 1 during the test. Comparison between the three considered punch penetrations: p=1 p_f, p=0.75 p_f and p=0.5 p_f.

The influence of the punch penetration value on the springback is shown in Figure 4.15. Both the intermediate and full penetrations have similar springback angles, differing only in the punch contact area. On the other hand, the springback predicted for the lower penetration value is considerably different from those two. The springback angle is 80.9° for the lower penetration case, while for the two remaining cases is 87.8°, representing an increase of about 9%.

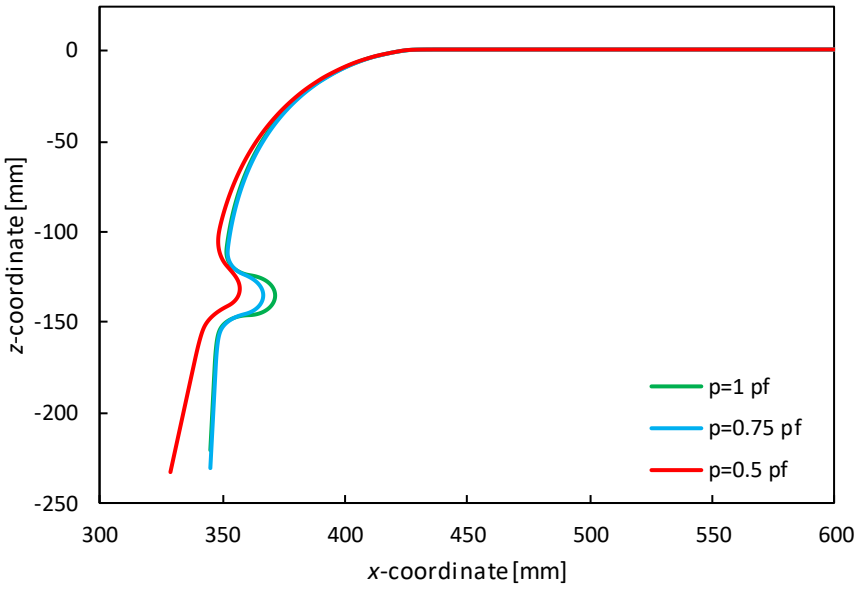

Figure 4.15. Springback of the blank. Comparison between the three different punch penetrations: p=1 p_f, p=0.75 p_f and p=0.5 p_f.

Since the springback is caused by the stress state in the blank before the load removal, the stress gradient in the thickness direction is directly related with the increase of the springback (Rodrigues and Martins, 2010). The difference between the springback of the lower penetration and the others is a consequence of the different stress gradients in the thickness direction, along the strip. In this case, the through-thickness stress gradient was evaluated in a section of the blank representative of the steady regime. Figure 4.16 presents the normal stress component, with respect to the rolling direction, σ_{11}, as well as the EPS, both calculated at the six Gauss points (GP) present in the thickness direction. The reference through-thickness position is calculated based on the average distance between the higher GP and lower GP. The upper surface is subjected to compression stress, while the lower surface is under tension stress (see Figure 4.16 (a)). The neutral line is slightly deviated from

the middle line, due to the normal stress imposed by the grip displacement, which is added to the bending stress, resulting in σ_{11}. The stress gradient is slightly bigger (6%) for the intermedium and higher punch penetrations, in comparison with the lower penetration. This is the cause for the differences in the springback, despite both cases showing higher EPS values. In fact, the main differences in the EPS between all cases are near the blank surface, because in the centre of the blank thickness it is quite small for all cases (between 0.01 and 0.02), as shown in Figure 4.16 (b).

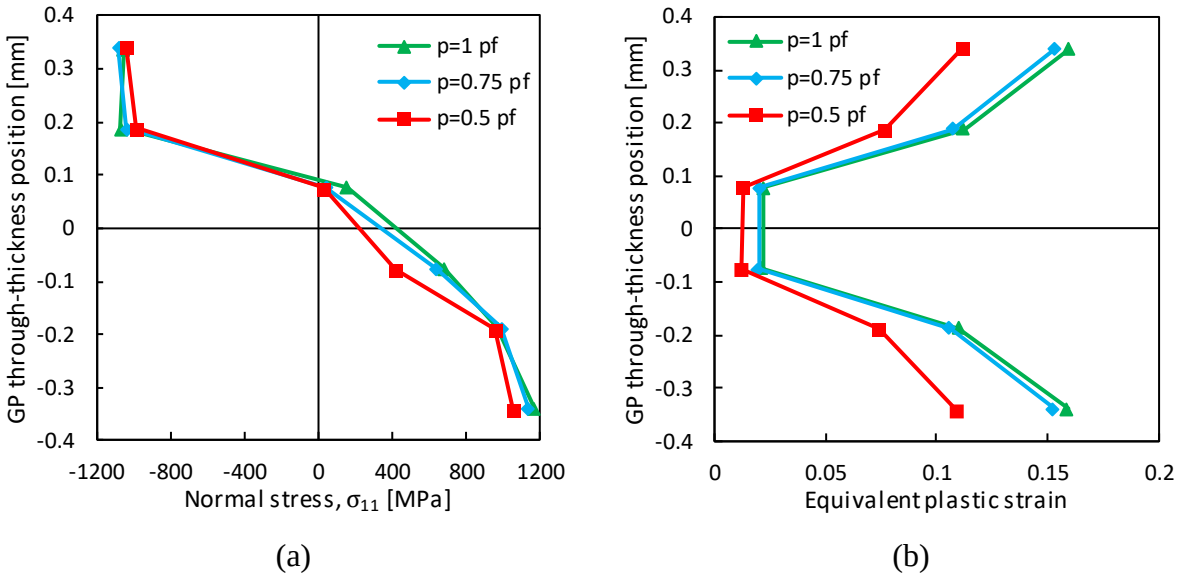

Figure 4.16. Distribution of stress and strain in the Gauss points located in the thickness direction located at a section representative of the steady state regime (grip displacement of 112.5 mm): (a) normal stress σ_{11} in the rolling direction; (b) equivalent plastic strain. Influence of punch penetration.

The influence of the punch penetration is more evident in the forces and contact angles. Regarding the forces, the punch displacement dictates the magnitude of the forces, not only in the *z*-direction but also in the *x*-direction. The contact angles are significantly reduced when the penetration is inferior, being the contact angle value directly related to the displacement of the punch. Comparing the contact angle and the EPS, which is bigger for the higher values of punch penetration, the temperature of the blank rises with the decrease of the penetration, leading to the conclusion that the temperature is more influenced by the contact angle (area) than by the equivalent plastic strain generated during the punch displacement, i.e. the heat lost by conduction is quite relevant in this test.

4.3. Side clearance

In this section, the influence of the side clearance (gap) on the evaluated process conditions (forces, temperatures and contact angles) is studied. Thus, four numerical simulations were performed, assuming 0.8 mm, 1 mm, 1.2 mm and 1.6 mm of side clearance, corresponding to 1 (g=1 t_0), 1.25 (g=1.25 t_0), 1.5 (g=1.5 t_0) and 2 (g=2 t_0) times the blank initial thickness, t_0, respectively.

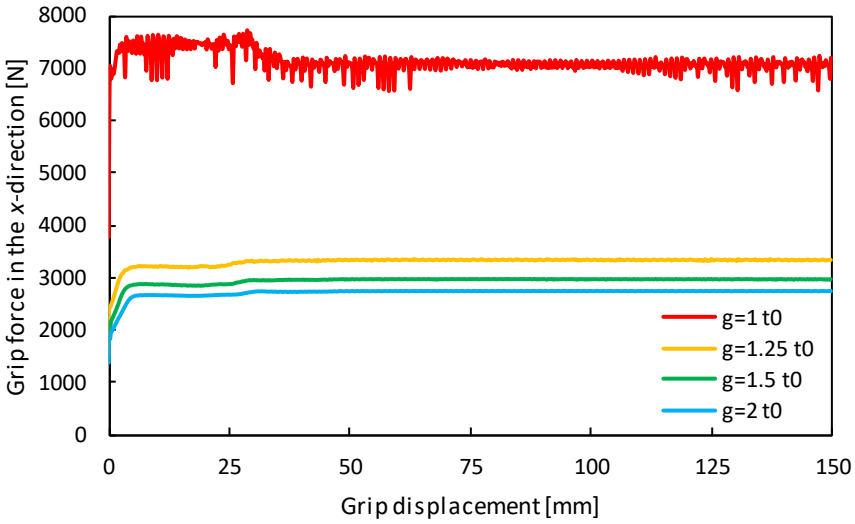

Figure 4.17. Grip force evolution for the four different values of side clearance.

Figure 4.17 presents the grip force, G_x, during the second phase (grip displacement), comparing the four values of side clearance. The force increases with the decrease of the side clearance, since the blank becomes increasingly more constrained. There is a clear difference between the lower gap and the remaining cases. In fact, the value of G_x obtained for 0.8 mm gap (g=1 t_0) is more than the double of the force obtained for 1 mm gap (g=1.25 t_0), reaching the value of approximately 7130 N. Indeed, comparing to the value of 3290 N obtained for the 1.25 t_0 gap it represents an increase of about 117%. The achieved grip forces for the 1.5 t_0 and 2 t_0 gap values are 2950 N and 2700 N, respectively. The fluctuations verified in the grip force for g=1 t_0 case (Figure 4.17) are due to the numerical treatment of the contact between the blank and the tools, which is performed with a node-to-segment approach.

The evolution of the punch force in the z-direction, P_z, during the first phase is presented in Figure 4.18 (a). The force evolution is similar in all cases until the displacement

of approximately 16mm. After that, the punch force for the lower gap increases significantly, reaching the maximum value of 6440 N. For the remaining gap values, the forces are quite similar, showing a difference of less than 300 N between the maximum values. The maximum force value for the g=1.25 t_0, g=1.5 t_0 and g=2 t_0 cases are 2620 N, 2350 N and 2120 N, respectively.

The evolution of the punch force in the z-direction, P_z, during the second phase (grip displacement) is presented in Figure 4.18 (b). As expected, the higher forces occur for the lower side clearance, reaching the maximum value of 6200 N. Similar to the first phase, there a considerable difference in the magnitude of P_z between the g=1 t_0 and the remaining cases. The behaviour of the vertical punch force is in agreement with the grip force (see Figure 4.17), reaching a steady state for higher than 37.5 mm of displacement. The achieved force values for the g=1.25 t_0, g=1.5 t_0 and g=2 t_0 cases are 2780 N, 2520 N and 2310 N, respectively.

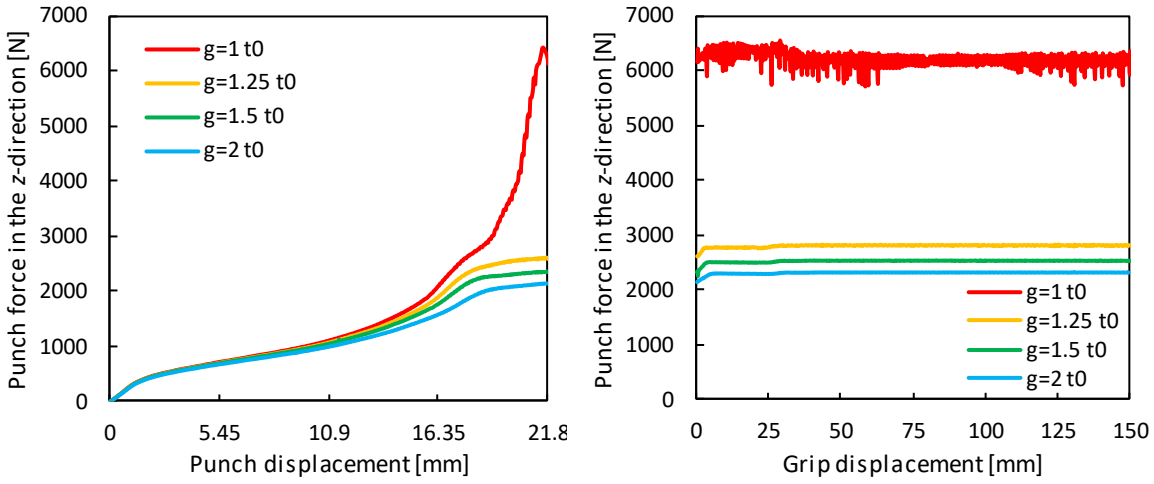

Figure 4.18. Evolution of the punch force in the z-direction for the four values of side clearance: (a) during the punch displacement; (b) during the grip displacement.

Concerning the influence of the side clearance on the contact angles θ_1, θ_2 and θ_3, the same approach considered in Section 4.3 is used, i.e. the angle values are measured during the steady state regime (grip displacement of approximately 112.5 mm). Figure 4.19 presents the three contact angles for the four gap values adopted in this study. The angles generally increase with the decrease of the side clearance, reaching the maximum values of

68.9°, 174.4° and 72.7° for θ_1, θ_2 and θ_3, respectively, in the g=1 t_0 case. All angles vary in the same way with the gap, as expected, since the punch becomes increasingly embraced by the blank when the left and right dies reduce their distance to the punch. The angles most affected by the gap distance are θ_1 and θ_2, showing a bigger decrease as compared to θ_3, when the gap increases (average decrease of 18°, while for θ_3 is about 10°).

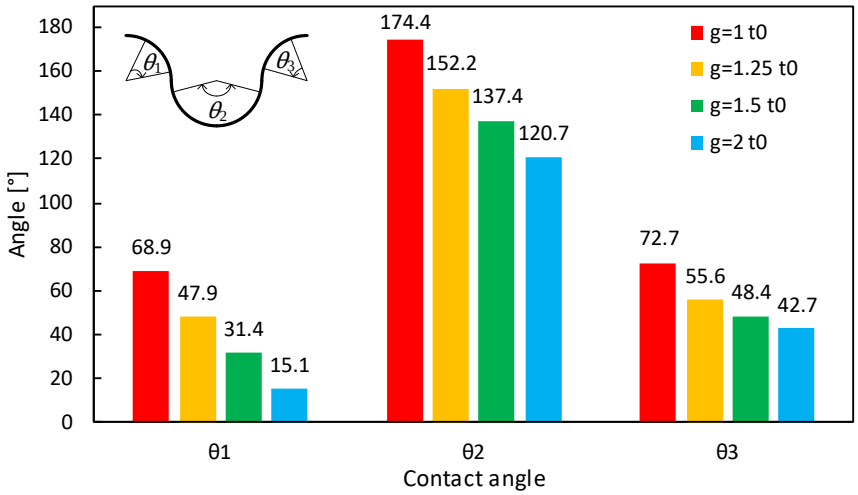

Figure 4.19. Contact angles θ_1, θ_2 and θ_3 for a grip displacement of 112.5 mm. Comparison between g=1 t_0, g=1.25 t_0, g=1.5 t_0 and g=2 t_0.

Figure 4.20 presents the temperature distribution at the end of the grip displacement, comparing four values of side clearance. The maximum temperature achieved is 303.9 K, corresponding to the g=1 t_0 case. The maximum temperature value for the lower gap occurs in the transition zone between the left die and the punch, while for the remaining cases the maximum temperature occurs in the zone at the exit of the right die. Despite the equivalent plastic strain being very similar between the 1 mm (g=1.25 t_0), 1.2 mm (g=1.5 t_0) and 1.6 mm (g=2 t_0) gaps, the temperature is lower for the first case, due to the bigger contact area with the tools (Figure 4.19), which imposes more heat losses (see Figure 4.20). Indeed, the temperature for g=1.25 t_0 case is 302.1 K while for the two remaining gap values is 302.6 K. The locations of the temperature peaks do not match due to the different contact angles and to the positioning of the left and right dies with respect to the punch.

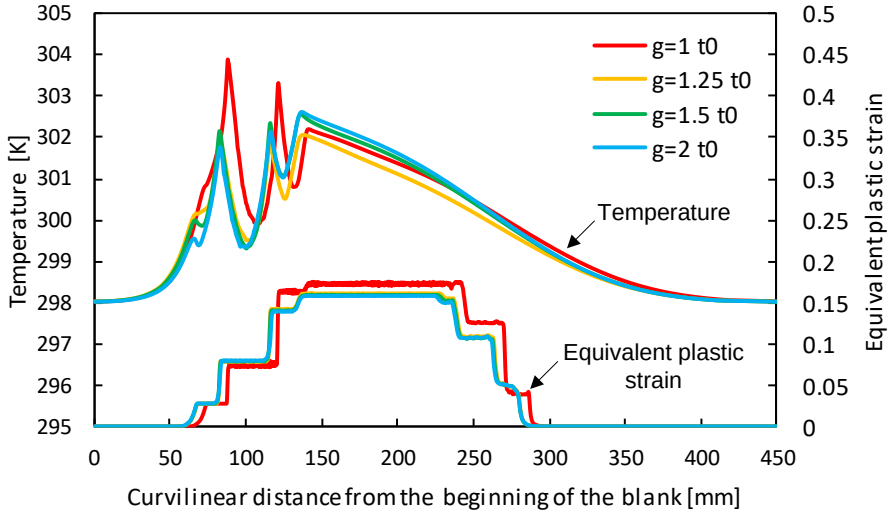

Figure 4.20. Temperature and equivalent plastic strain distributions obtained at the end of the grip displacement. Comparison between the considered gap distances: g=1 t_0, g=1.25 t_0, g=1.5 t_0 and g=2 t_0.

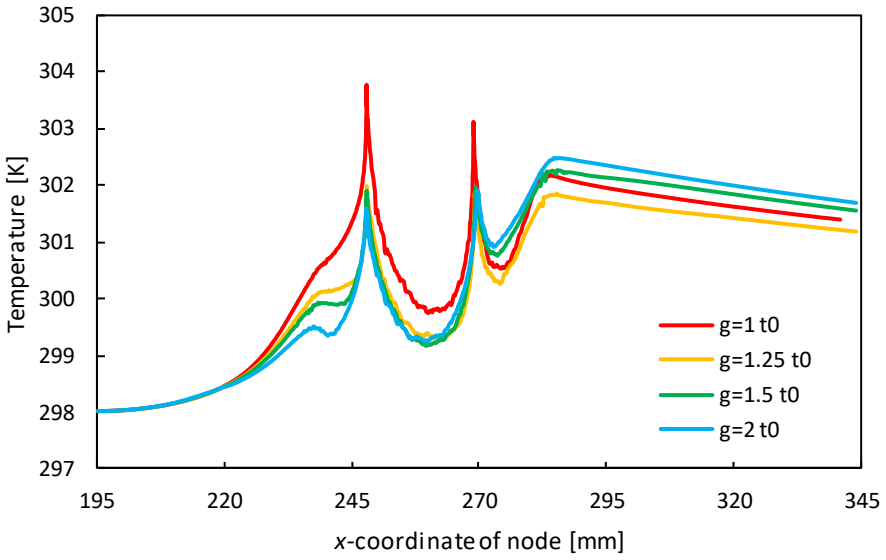

Figure 4.21. Temperature evolution in node 1 during the test. Comparison between the considered gap distances: g=1 t_0, g=1.25 t_0, g=1.5 t_0 and g=2 t_0.

Figure 4.21 shows the temperature evolution for the reference node (node 1). All gap values show similar evolution, with peaks at approximately the same locations, i.e. in the transition zones between the dies and the punch and at the end of the contact with the right die. The maximum temperature achieved for node 1 is 303.8 K, which occurs for the lowest gap distance. When considering the g=1.25 t_0, g=1.5 t_0 and g=2 t_0 cases, the larger temperature occurs for the latter, due to the combined effect of the lower contact area with the tools and similar EPS.

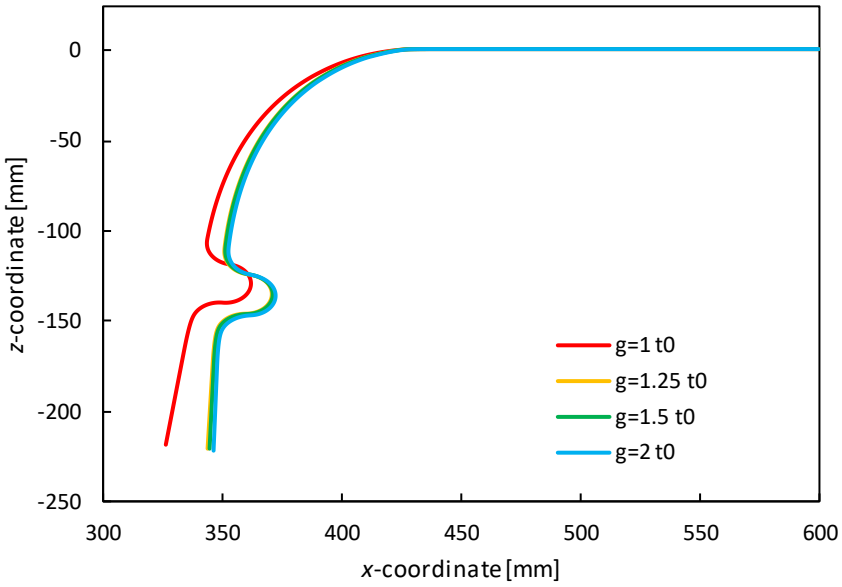

Figure 4.22. Springback of the blank for different values of gap distance: g=1 t_0, g=1.25 t_0, g=1.5 t_0 and g=2 t_0.

Figure 4.22 presents the springback for the different gaps distances. It is noticeable that the springback angle is similar for g=1.25 t_0, g=1.5 t_0 and g=2 t_0, while for g=1 t_0 there is a slight decrease in the angle, reducing from approximately 87.8° to 78.9°. Since the stress state within the blank is the dominant factor in the springback (Li et al., 2002), the normal stress with respect to the rolling direction is also studied for the cases under analysis. Figure 4.23 (a) presents the normal stress in the thickness direction (for a section located in the zone corresponding to steady state), calculated for the six Gauss Points (GP) comprised in the three finite elements considered. The stress gradient in the g=1 t_0 case is about 8% inferior than the one obtained with the remaining gap values (very similar stress gradients), resulting in a lower springback angle (10% lower than the remaining cases). Figure 4.23 (b) shows the equivalent plastic strain calculated for the six GP. The difference occurs for the g=1 t_0 case, especially in the centre of the blank, as in the surface the EPS values are very similar for all gap values. Indeed, in the centre of the blank the EPS for the g=1 t_0 is approximately 0.08. Comparing to the remaining cases (0.02) it represents an increase of about 3.5 times in the EPS, which also contributes to the differences noticed in the springback.

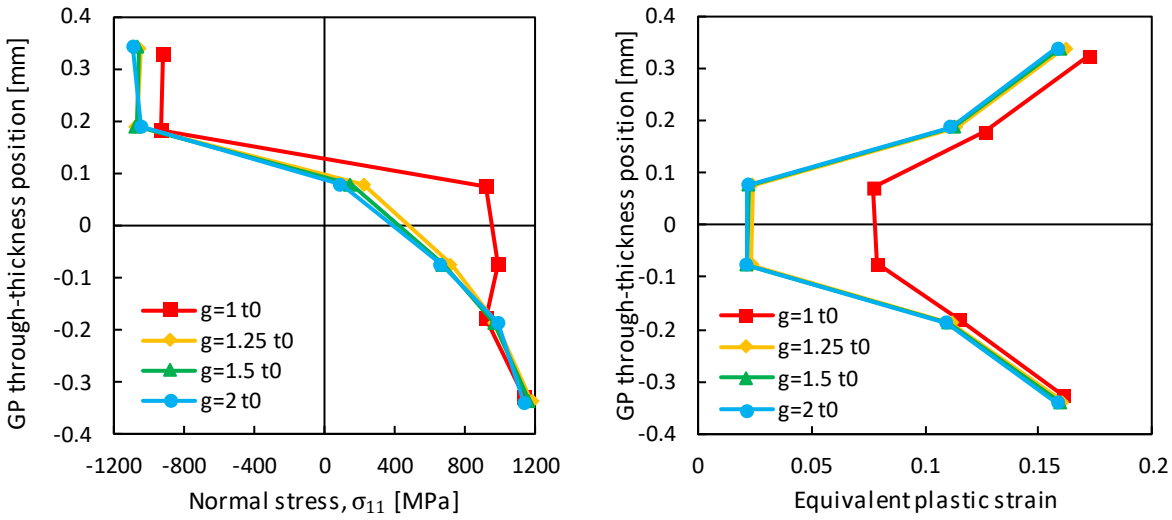

Figure 4.23. Evolution of the punch force in the *z*-direction, P_z, for the four values of side clearance: (a) during the punch displacement; (b) during the grip displacement.

As main conclusion, the gap value presents a strong impact on the predicted forces and contact angles. Regarding the forces, the decrease of the gap results in higher forces, with a substantial increase for gap values close the blank thickness (increase of about 117% in G_x and 146% in P_z, between the 1 mm and the 0.8 mm gaps). Attention must be given to the arising of numerical instabilities related to the contact between the blank and the tools for the latter case. The contact angles increase for gaps closer to the sheet thickness. In fact, for the g=1 t_0 case, the overall contact angle ($\theta_1+\theta_2+\theta_3$) almost matches the wrap angle considered by (Nine, 1978) to evaluate the friction coefficient, reaching the maximum value of 316°.

4.4. Friction coefficient

In this section, the influence of the friction coefficient μ on the predicted forces, temperatures and contact angles is studied. Thus, five numerical simulations were performed, considering values of 0.00, 0.05, 0.10, 0.15 and 0.20 for the friction coefficient.

Figure 4.24 presents the evolution of the punch force with the increase of μ during both the first phase (punch displacement) and the second phase (grip displacement). The effect of the friction coefficient on the behaviour of the forces is very similar for all cases, with forces increasing for higher friction coefficient values. As mentioned in Section

4.2, there is a slight increase in the punch force value during the second phase (before reaching the steady state regime). The force increases from 1630 N verified in the frictionless case to 2940 N, that occur for μ=0.2. In fact, the force increases for each increment of the friction coefficient approximately 15% (during the second phase).

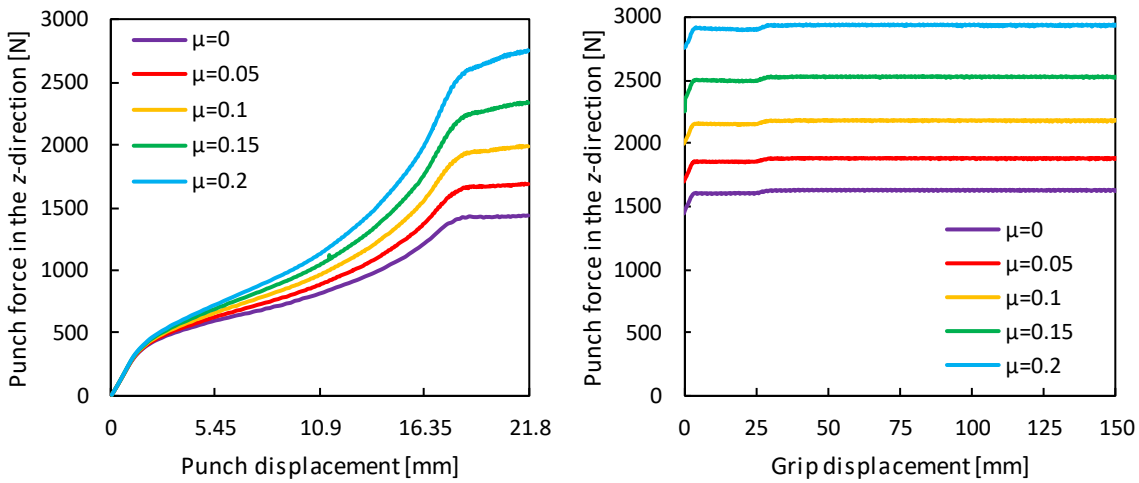

Figure 4.24. Evolution of the punch force for the studied friction coefficients: (a) during the punch displacement; (b) during the grip displacement.

Figure 4.25 show the grip forces during the second phase for the five tested values of μ. The grip force shows a behaviour similar to the punch force with the increase of μ, i.e. is higher for superior values. The force increases about 20% for each increment of μ, from 1690 N (frictionless case) to 3650 N, which is obtained for the higher friction value of 0.2.

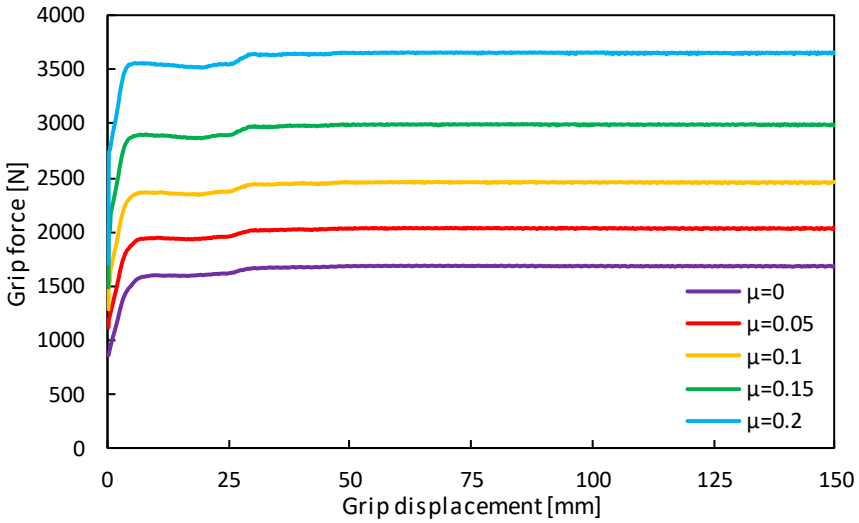

Figure 4.25. Grip force evolution for the five values of friction coefficient.

Regarding the contact angles, Figure 4.26 shows the behaviour of θ_1, θ_2 and θ_3 for the different friction coefficient values. θ_1 and θ_2 are almost insensitive to the friction coefficient, differing less than 3°, presenting values around 32° and 137°, respectively. The influence of the friction coefficient is more pronounced on θ_3, which increases about 13° from the frictionless case to the μ=0.2 case. The overall contact angle ($\theta_1+\theta_2+\theta_3$) increases approximately 19° considering the larger value of friction coefficient (μ=0.2) in comparison with the frictionless case.

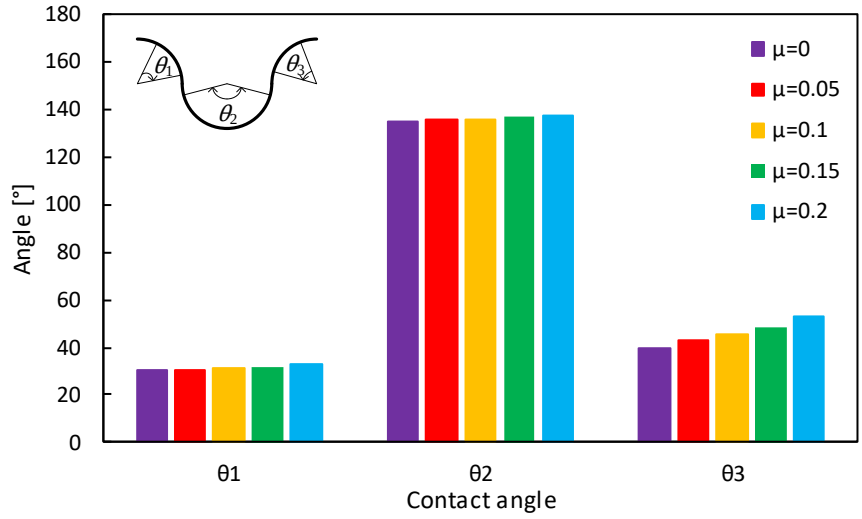

Figure 4.26. Contact angles θ_1, θ_2 and θ_3 for a grip displacement of 112.5 mm. Comparison between μ=0, μ=0.05, μ=0.1, μ=0.15 and μ=0.2.

Figure 4.27 presents the temperature and equivalent plastic strain (EPS) distributions at the end of the second phase (grip pulling). The EPS is not affected by the friction coefficient value adopted in the numerical model. Since the effect of friction on the EPS distribution is negligible and the contact angles are almost the same (see Figure 4.26), the predicted temperatures for the different μ values are very similar. Indeed, the larger difference in the predicted temperature occurs between the frictionless and μ=0.2 cases and it is lower than 0.4°.

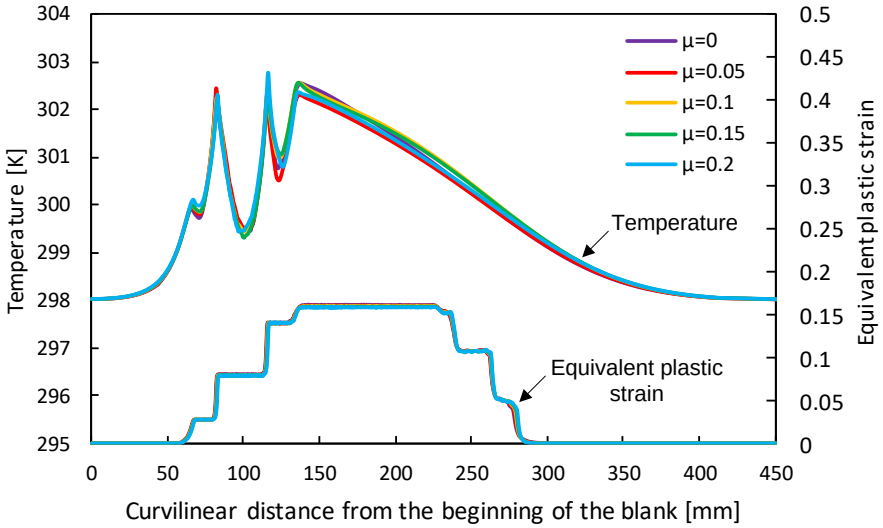

Figure 4.27. Temperature and equivalent plastic strain distributions obtained at the end of the grip displacement. Comparison between μ=0, μ=0.05, μ=0.1, μ=0.15 and μ=0.2.

In order to predict the friction coefficient between the blank and the tools in the draw bead test, (Nine, 1978) proposed two analytical methods, one considering constant contact pressure and another considering linear increase of the pressure. In both cases it is assumed that the overall contact angle ($\theta_1+\theta_2+\theta_3$) is 360°. In this study, the two methods are adopted to predict and compare the global friction coefficient with the one used as input for the numerical simulations. Considering constant contact pressure, the analytical prediction of the friction coefficient is given by:

$$\mu_p = \frac{G_{d+f} - G_d}{\pi P_{d+f}}, \tag{4.1}$$

where G_{d+f} and P_{d+f} are the grip and punch forces, respectively, considering both the load due the deformation (bending of the blank) and frictional forces. G_d represents the grip force for the frictionless case (μ=0), i.e. considering only the bending component. The analytical model that assumes a linear increase of the contact pressure leads to a prediction of the friction coefficient with the form:

$$\mu_p = \frac{-b \pm \sqrt{b^2 - 4ac}}{2a}, \text{ with } \begin{cases} a = \pi G_d + (\pi - 2) P_d \\ b = (\pi - 2) G_d - (\pi - 2) G_{d+f} / 2 + 2\pi P_{d+f} \\ c = \pi (G_d - G_{d+f}) + (\pi - 2)(P_{d+f} - P_d) \end{cases} \tag{4.2}$$

where P_d is the punch force for the frictionless case. Both models assume that the test is performed until attaining steady state conditions, to enable the proper evaluation of the forces.

Table 4.2 presents the values of the forces (punch and grip) predicted by numerical simulation at the steady state instant, considering various values of μ. These values were applied in Equation (4.1) and Equation (4.2) to estimate the friction coefficient, for both constant and linear increase of the contact pressures, respectively.

Table 4.2. Grip and punch forces achieved in the draw bead test for the five tested friction coefficient values: μ=0, μ=0.05, μ=0.1, μ=0.15 and μ=0.2. G_d and P_d represent the forces for frictionless case. G_{d+f} and P_{d+f} are forces related to the frictional contact with the tools.

μ	G_d [N]	G_{d+f} [N]	P_d [N]	P_{d+f} [N]
0	1690	–	1630	–
0.05	–	2030	–	1880
0.1	–	2450	–	2180
0.15	–	2980	–	2530
0.2	–	3650	–	2940

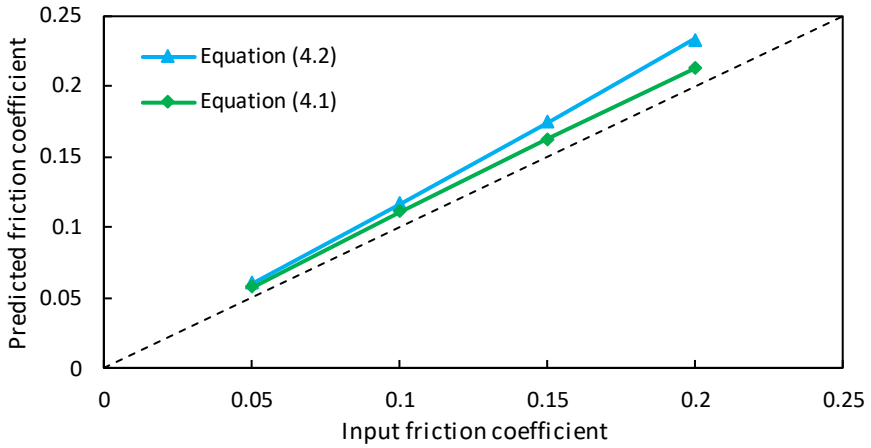

Figure 4.28. Predicted friction coefficient calculated by Equation (4.1) and Equation (4.2), considering constant contact pressure and linear increase of the contact pressure, respectively, for the μ=0, μ=0.05, μ=0.1, μ=0.15 and μ=0.2 values.

Figure 4.28 presents the predicted friction coefficient, calculated using both analytical models, for the studied values of μ. Both analytical models lead to an overestimation of the predicted friction coefficient, which is in agreement with the results by (Oliveira et al., 2011) for similar gap distances. The error is higher when adopting

Equation (4.2), particularly for higher values of friction coefficient. Indeed, Equation (4.1) yields more accurate results for the considered gap and punch penetration (g=1.5 t_0 and p=p_f). The discrepancy between the input friction value and the predicted is due to the contact pressure neither being constant or increasing linearly throughout the contact. Besides, the contact angle is not 360° (see Figure 4.26), which is the overall contact angle considered in both analytical models. Figure 4.29 shows the nodal contact forces under steady state conditions. The pressure is neither constant nor linearly increasing in the contact area with the tools, while the overall contact angle is always inferior to 360°, clarifying the discrepancies mentioned above.

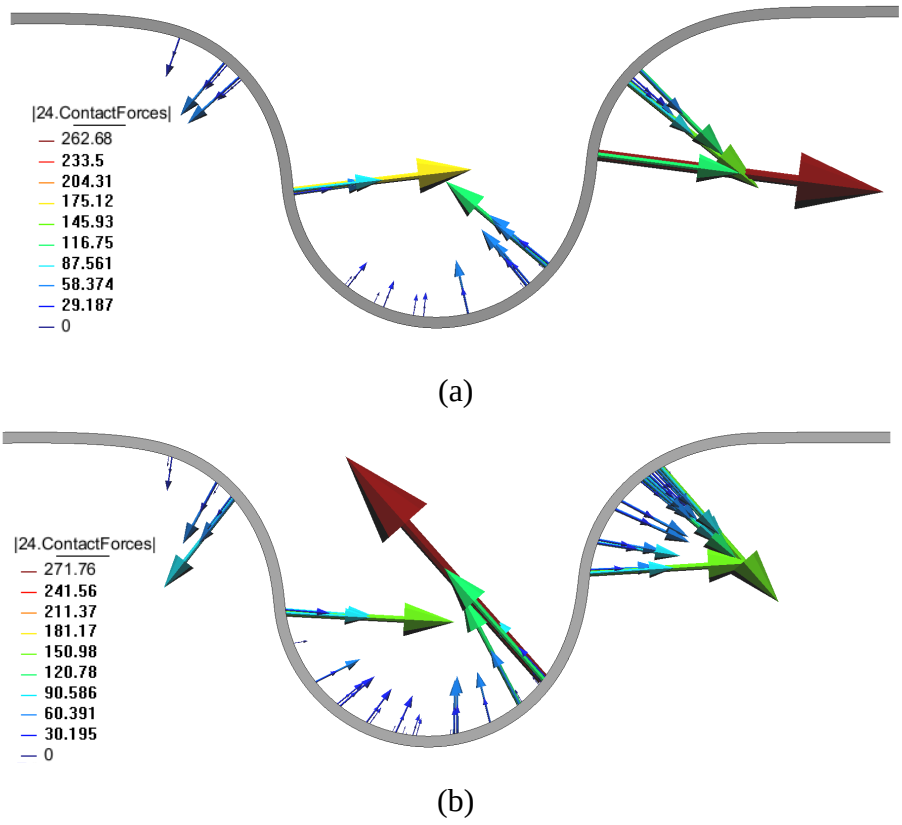

Figure 4.29. Nodal contact force distribution under steady state conditions, evaluated for the case of 1.2 mm of gap (g=1.5 t_0) and full penetration (p=1 p_f): (a) Frictionless conditions (μ=0); (b) Friction coefficient of 0.2.

The impact of the friction coefficient on the equivalent plastic strain and consequently on the temperature is almost negligible. Thus, heat generated by frictional sliding is very low in comparison with the one generated by plastic strain. On the other hand, the friction coefficient has a significant impact on the predicted forces, presenting

approximately a linear relation with the magnitude of the punch and grip forces evolutions. The increase of the friction coefficient leads to a slight increase of the contact angles, which is about 3° for θ_1 and θ_2, and about 13° for θ_3.

4.5. Material

In this section, the influence of the mechanical properties of the blank material is studied, as well as the effect of the grip speed during the pulling operation. Thus, both dual phase steels are considered (DP780 and DP500), which are modelled according to the mechanical behaviour presented in Section 2.2.1. The impact of the material on the predicted forces, temperatures, contact angles and springback is assessed.

Figure 4.30 and Figure 4.31 show the force evolution of the punch and the grip, respectively, for both materials. The forces show a similar behaviour, differing only in their magnitude. Regarding the evolution of the punch force, the DP780 reaches a maximum value of 2340 N when the force stabilizes at around 30 mm of grip displacement, due to the higher strength of the DP780 (see Figure 2.2). On the other hand, the DP500 achieves 1720 N, which represents a difference of about 32% (see Figure 4.30 (b)). Indeed, the strength of the DP780 is approximately 36% higher than the DP500 (for an EPS of 0.15), which relates to the predicted differences in the forces.

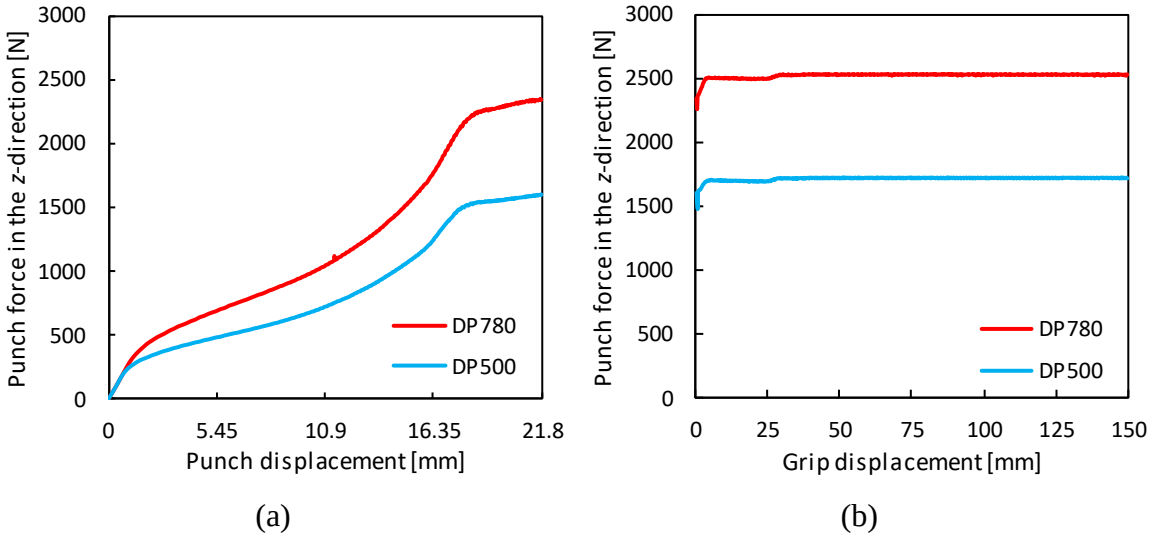

Figure 4.30. Evolution of the punch force for the DP780 and DP500 steels: (a) during the punch displacement; (b) during the grip displacement.

The grip force stabilizes at the same grip displacement (30 mm) and, like the punch force, achieves the maximum value for the DP 780, reaching 2980 N. On the other hand, the grip force is 2050 N for the DP500. Comparing both values, there is a difference of approximately 31% (see Figure 4.31).

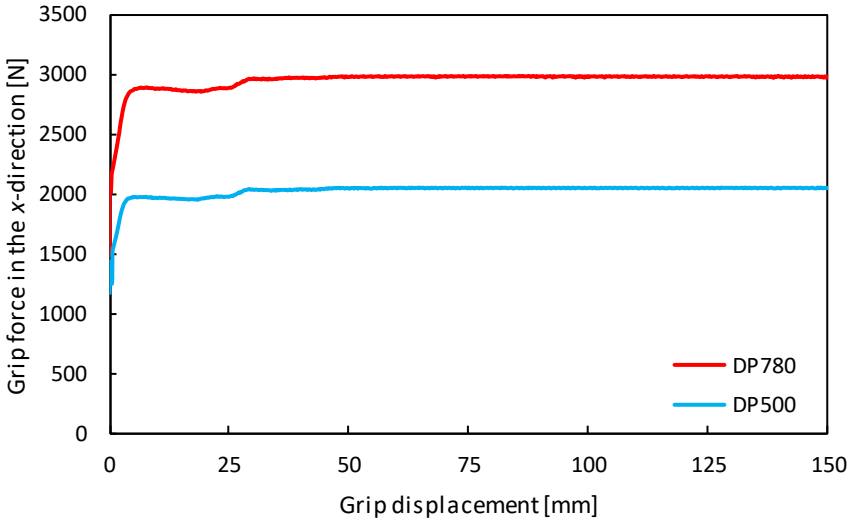

Figure 4.31. Evolution of the grip force during the second phase (grip pulling). Comparison between DP780 and DP500.

Fig 4.32 presents the contact angles for each material (DP500 and DP780). The contact angles are also slightly higher for the DP780, increasing approximately 8°, 6° and 3° for θ_1, θ_2 and θ_3, respectively, reaching 31.4°, 137.4° and 48.4°. On the other hand, the angles observed for the DP500 are 23.6°, 131.7° and 45.9°, for the previously mentioned contact angles. This slight difference can result from the slightly lower *r*-values for the DP780 in comparison with the DP500 (see Table 2.2).

Figure 4.33 presents the distributions of temperature and EPS for both materials at the end of the grip displacement, considering 1 mm/s of pulling velocity. The increase of the global value of the temperature for the DP780 is explained by the difference in the flow stress (Figure 2.2) of both materials. Although the EPS predicted for the DP780 is about 10% less than for the DP500 (see Figure 4.33), the flow stress attained for these values of EPS is significantly higher for the DP780. The heat generated by plastic deformation takes into account the plastic power (see Equation (3.4)), which can be related with the plastic work, i.e. the product between the equivalent stress and the equivalent plastic strain. Thus, it is expected to predict higher temperatures for materials with higher flow stress (equivalent stress). Indeed, the DP780 presents an increase of 1 K in the temperature. The influence of

the contact angle is almost negligible in this range, as mentioned in Section 4.4. The maximum temperature achieved for the DP780 is 302.6 K, while for the DP500 is 301.6 K.

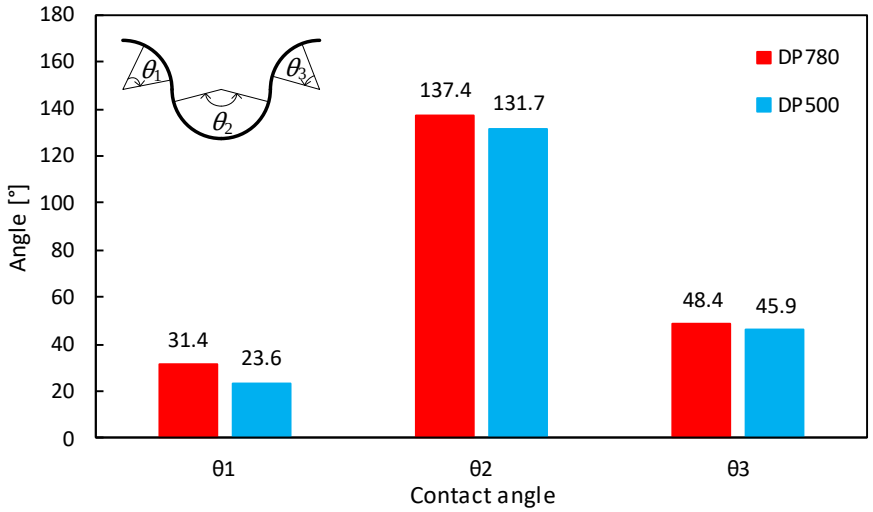

Figure 4.32. Contact angles θ_1, θ_2 and θ_3 for a grip displacement of 112.5 mm. Comparison between DP780 and DP500.

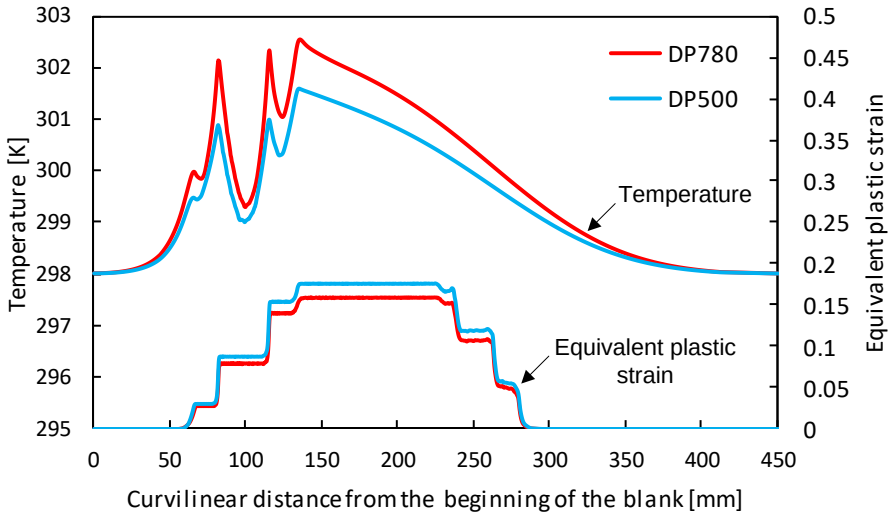

Figure 4.33. Temperature and equivalent plastic strain distributions obtained at the end of the grip displacement (1mm/s). Comparison between DP780 and DP500.

The influence of the material properties on the springback is shown in Figure 4.34. The springback predicted for the DP500 is lower than the one predicted for the DP780. The springback angle of the DP500 is 73.9°, while for the DP780 is 87.8°, which corresponds to a difference of about 16%. This results from the through-thickness stress state observed, particularly in the region of the blank corresponding to the steady state regime. Figure 4.35

presents the normal stress with respect to the rolling direction and the EPS, calculated for the six Gauss points in the thickness direction. Although the DP500 presents larger EPS values (see Figure 4.35 (b)), the stress gradient in the thickness direction is significantly lower (see Figure 4.35 (a)). In fact, the stress gradient predicted for DP500 is approximately 32% lower than the one predicted for the DP780 steel, resulting in a springback angle approximately 16% inferior (see Figure 4.34).

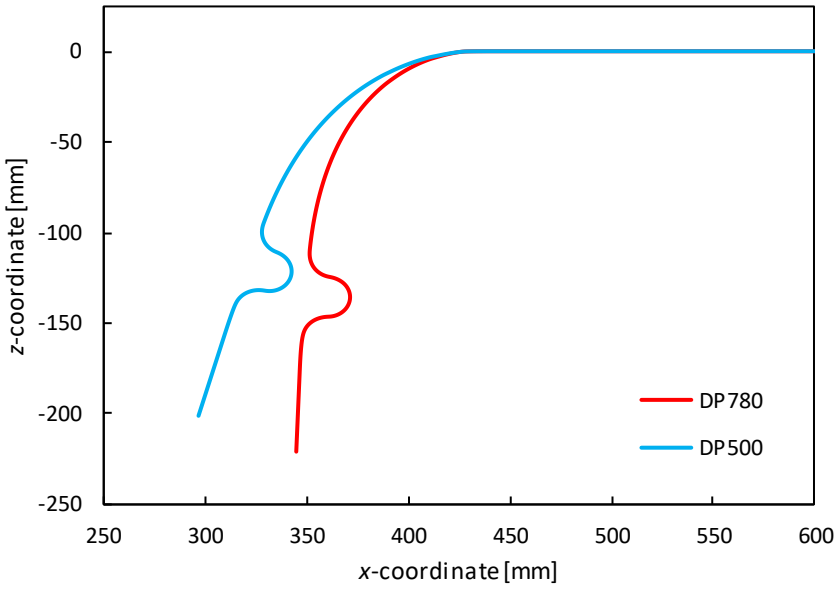

Figure 4.34. Springback of the blank. Comparison between the two different materials: DP500 and DP780.

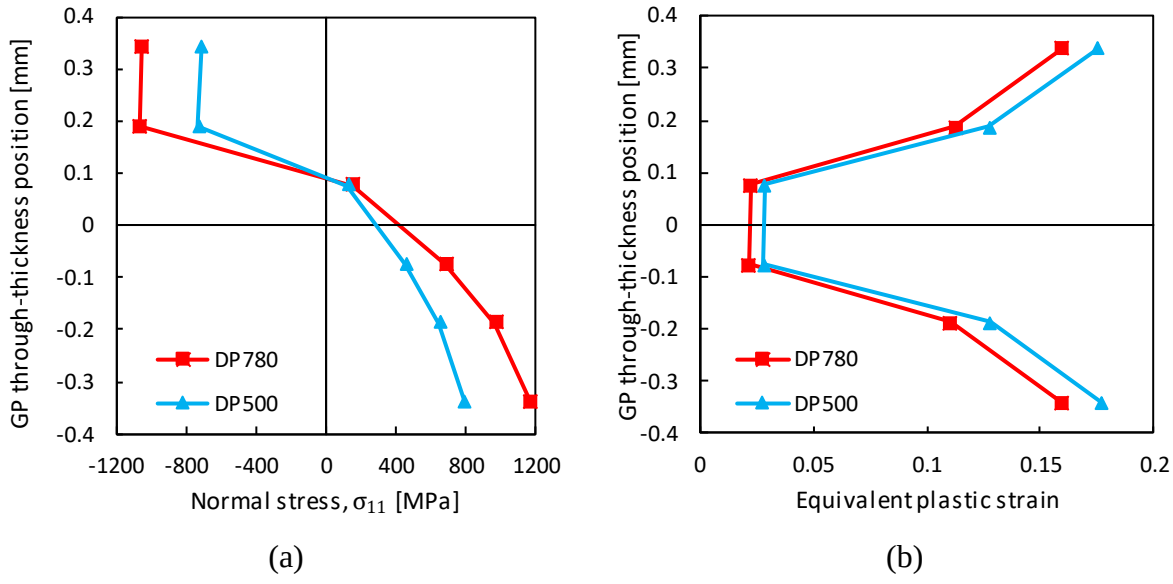

Figure 4.35. Gauss points located in the thickness direction located at a steady state regime (grip displacement of 112.5 mm). Comparison between DP780 and DP500 regarding: (a) normal stress σ_{11} in relation to the rolling direction; (b) equivalent plastic strain.

The influence of the material properties is particularly noted in the forces and springback. The contact angles are residually affected by the change in the material properties. Since the DP780 has higher strength, the predicted temperature is higher than for the DP500 (about 1 K), although the later presents higher EPS values. The punch force and grip force diminish almost 30%, the EPS augments 10% on the blank surface and the springback angle reduces 16% when the DP500 steel is used.

4.6. Pulling speed

To assess the effect of the pulling velocity on the predicted temperature, additional simulations were performed considering 10 and 20 mm/s of grip velocity for the DP780 steel. With the increase of the velocity, the heat fluxes due to frictional forces and plastic deformation increase as well (see Equation (3.4) and Equation (3.11)). The thermal heat energy (work) generated by both fluxes is the same regardless of the test velocity. Indeed, the increase of the velocity reduces the total time of the test, which means that the same work will be performed in a smaller time period. Thus, the temperature rise is explained by the heat losses and the conduction within the blank, which are also time-dependant. Since there is less time, there is less heat loss to the tools and the environment, increasing the overall blank temperature. Due to the reduction of the time period, the conduction effect within the blank also becomes negligible, as mentioned in Section 3.3.1.

Figure 4.36 presents the temperature distribution at the end of the grip displacement for the three velocities. As expected, the temperature is maximum for the higher velocity (v=20mm/s), reaching 322.5 K. For this test, the temperature rises from 302.6 K to 317.3 K. Between the lower and intermedium velocities there is an increase of 14.7 K. The temperature difference between the higher and lower velocities is approximately 20 K, which denotes a large influence of the pulling velocity in the predict temperature. The influence of the pulling velocity reveals great influence on the temperature of the blank, increasing the temperature approximately 15 K when the pulling speed increases from 1 mm/s to 10 mm/s and approximately 20 K for a velocity of 20 mm/s.

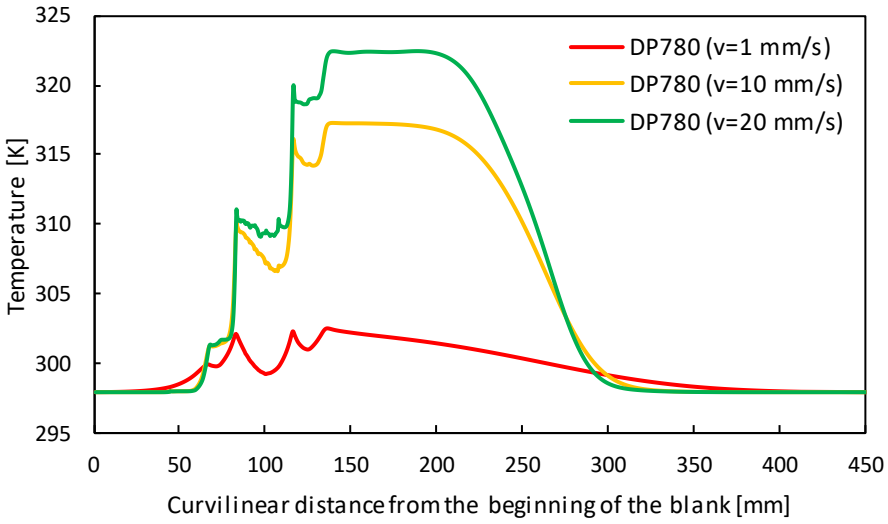

Figure 4.36. Temperature distributions of the DP780 steel obtained at the end of the grip displacement. Comparison between v=1mm/s, v=10mm/s and v=20mm/s.

5. Conclusions

With the development of the automotive industry, advanced high-strength steel sheets are becoming very common in stamping processes (Kuziak et al., 2008). However, their higher strength also requires improved knowledge since this can be a decisive factor for the correct description of a given forming process. Further, the numerical modelling of this forming process can require a coupled thermo-mechanical approach due to the thermal softening. Thus, the main goal of this work was the numerical study of the contact with frictional conditions involved in the draw bead test, with particular focus on the thermal problem.

In order to study the draw bead test, a thermomechanical finite element model was developed, which considers both the heat transfer to the tools (IHTC) and for the environment, as well as heat generated by plastic deformation and friction. The effect of the main process parameters was assessed, in particular the penetration of the punch, the side clearance between the tools, the coefficient of friction, the material of the blank and pulling speed of the grip. In addition to the temperature, the process parameters (forces, stresses, strains, contact angles and springback) were also studied, considering a model that comprises plane strain conditions.

The process parameters with the biggest influence on the temperature of the blank were the pulling speed and the punch penetration, followed by the side clearance. The influence of the pulling velocity on the predicted temperature is very high. In fact, for velocities of 10 and 20 mm/s the temperature variation increases from 19.3 K to 24.5 K, respectively, reaching the maximum values of 317.3 K and 322.5 K. Regarding the punch penetration, the temperature of the blank rises when the penetration is lower. Despite the lower EPS value generated, the reduced contact area with the tools leads to a temperature increase due to the reduced heat loss. Indeed, the maximum temperature achieved was 304.6 K, corresponding to an increase of 6.6 K, for the lower punch displacement (p=0.5p_f). Finally, the influence of the side clearance on the temperature was particularly noted for the lower gap (0.8 mm), with the temperature increasing 5.9 K, reaching the maximum value of 303.9 K.

The influence of the friction coefficient on the temperature rise is negligible. Nevertheless, the contact forces are especially influenced by the coefficient of friction, while the contact angles depend mainly on the punch penetration. Thus, the heat generated by the friction forces during the sliding is significantly lower than the one resulting from the plastic strain. Hence, the speed of the grip is the main process parameter affecting the blank temperature rise, due to the reduction of the time period for the occurrence of heat losses to the environment and for conduction within the blank.

Globally, the results presented highlight the strong dependence of the thermal analysis of several parameters, such as the ones characterizing the heat transfer (e.g. IHTC and HTC). Thus, the use of the draw bead test to improve the model describing the heat generated by plastic deformation or contact with friction, requires also an improved understanding of the thermal parameters.

Bibliography

Altan, T., Tekkaya, A.E., 2012a. Sheet metal forming : process and applications. ASM International.

Altan, T., Tekkaya, A.E., 2012b. Sheet metal forming : fundamentals. ASM International.

Andrade-Campos, A., 2005. Modelação e Análise Numérica do Comportamento Mecânico e Térmico de Ligas de Alumínio. Universidade de Aveiro.

Ayres, R.A., Brazier, W.G., Sajewski, V.F., 1978. Evaluating the GMR-Limiting Dome Height Test as a new measure of press formability near plane strain. J. Appl. Metalwork. 1, 41–49. doi:10.1007/BF02833958

Bergman, T.L., Lavigne, A.S., Incropera, F.P., Dewitt, D.P., 2011. Fundamentals of Heat and Mass Transfer, 7th ed, Aerospace Engineering. Wiley. doi:10.1016/j.applthermaleng.2011.03.022

Ceretti, E., Braga, D., Giardini, C., Gerbino, G., 2010. Optimisation of Can Bottom Geometry by Means of Simulations. Int. J. Mater. Form. 3, 89–92. doi:10.1007/s12289-010-0714-3

Chang, Y., Tang, X., Zhao, K., Hu, P., Wu, Y., 2016. Investigation of the factors influencing the interfacial heat transfer coefficient in hot stamping. J. Mater. Process. Technol. 228, 25–33. doi:10.1016/j.jmatprotec.2014.10.008

Dilmec, M., Arap, M., 2016. Effect of geometrical and process parameters on coefficient of friction in deep drawing process at the flange and the radius regions. Int. J. Adv. Manuf. Technol. 86, 747–759. doi:10.1007/s00170-015-8225-5

Francavilla, A., Zienkiewicz, O.C., 1975. A note on numerical computation of elastic contact problems. Int. J. Numer. Methods Eng. 9, 913–924. doi:10.1002/nme.1620090410

Hill, R., 1948. A Theory of the Yielding and Plastic Flow of Anisotropic Metals. Proc. R. Soc. London A Math. Phys. Eng. Sci. 193.

Hu, P., Ma, N., Liu, L., Zhu, Y.-G., 2013. The Introduction of Sheet Metal Forming Technology. pp. 1–14. doi:10.1007/978-1-4471-4099-3_1

Kang, B.-S., Son, B.-M., Kim, J., 2004. A comparative study of stamping and

hydroforming processes for an automobile fuel tank using FEM. Int. J. Mach. Tools Manuf. 44, 87–94. doi:10.1016/j.ijmachtools.2003.08.009

Kuziak, R., Kawalla, R., Waengler, S., 2008. Advanced high strength steels for automotive industry. Arch. Civ. Mech. Eng. 8, 103–117. doi:10.1016/S1644-9665(12)60197-6

Lee, B.., Keum, Y.., Wagoner, R.., 2002. Modeling of the friction caused by lubrication and surface roughness in sheet metal forming. J. Mater. Process. Technol. 130, 60–63. doi:10.1016/S0924-0136(02)00784-7

Li, K.P., Carden, W.P., Wagoner, R.H., 2002. Simulation of springback. Int. J. Mech. Sci. 44, 103–122. doi:10.1016/S0020-7403(01)00083-2

Losch, A., 2014. Sheet Metal Forming Lubricants, Encyclopedia of Lubricants and Lubrication. Springer Berlin Heidelberg, Berlin, Heidelberg. doi:10.1007/978-3-642-22647-2_230

Martins, J.M.P., Neto, D.M., Alves, J.L., Oliveira, M.C., Laurent, H., Andrade-Campos, A., Menezes, L.F., 2017. A new staggered algorithm for thermomechanical coupled problems. Int. J. Solids Struct. doi:10.1016/j.ijsolstr.2017.06.002

Menezes, L.F., Teodosiu, C., 2000. Three-dimensional numerical simulation of the deep-drawing process using solid finite elements. J. Mater. Process. Technol. 97, 100–106. doi:10.1016/S0924-0136(99)00345-3

Nasser, A., Yadav, A., Pathak, P., Altan, T., 2010. Determination of the flow stress of five AHSS sheet materials (DP 600, DP 780, DP 780-CR, DP 780-HY and TRIP 780) using the uniaxial tensile and the biaxial Viscous Pressure Bulge (VPB) tests. J. Mater. Process. Technol. 210, 429–436. doi:10.1016/j.jmatprotec.2009.10.003

Neto, D.M., Oliveira, M.C., Menezes, L.F., Alves, J.L., 2014. Applying Nagata patches to smooth discretized surfaces used in 3D frictional contact problems. Comput. Methods Appl. Mech. Eng. 271, 296–320. doi:10.1016/j.cma.2013.12.008

Nine, H.D., 1982. New drawbead concepts for sheet metal forming. J. Appl. Metalwork. 2, 185–192. doi:10.1007/BF02834036

Nine, H.D., 1978. Drawbead Forces in Sheet Metal Forming, in: Mechanics of Sheet Metal Forming. Springer US, Boston, MA, pp. 179–211. doi:10.1007/978-1-4613-2880-3_8

Oliveira, M.C., Alves, J.L., Menezes, L.F., Ramalho, A., 2011. Finite Element Analysis of the Amontons-Coulomb's Model using Local and Global Friction Tests. pp. 1812–1817. doi:10.1063/1.3589779

P. Martins, J.M., Neto, D.M., Alves, J.L., Oliveira, M.C., Menezes, L.F., 2016. Numerical modeling of the thermal contact in metal forming processes. Int. J. Adv. Manuf. Technol. 87, 1797–1811. doi:10.1007/s00170-016-8571-y

Pereira, M.P., Yan, W., Rolfe, B.F., 2008. Contact pressure evolution and its relation to wear in sheet metal forming. Wear 265, 1687–1699. doi:10.1016/j.wear.2008.04.042

Rhee, S.K., 1974. Friction Coefficient of Automotive Friction Materials - Its Sensitivity to Load, Speed, and Temperature. doi:10.4271/740415

Rodrigues, J.M.C., Martins, P.A.F., 2010. Tecnologia Mecânica Vol. 1 - Tecnologia da Deformação Plástica, 2ª Edição. ed.

Taylor, G.I., Quinney, H., 1934. The Latent Energy Remaining in a Metal after Cold Working. Proc. R. Soc. London A Math. Phys. Eng. Sci. 143.

Teixeira-Dias, F., Pinho-da-Cruz, J., Fontes Valente, R.A., de Alves de Sousa, R.J., 2010. Método dos Elementos Finitos - Técnicas de Simulação Numérica em Engenharia. LIDEL.

Wagoner, R.H., Kim, J.H., Sung, J.H., 2009. Formability of advanced high strength steels. Int. J. Mater. Form. 2, 359–362. doi:10.1007/s12289-009-0644-0

Walczyk, D.F., Lakshmikanthan, J., Kirk, D.R., 1998. Development of a reconfigurable tool for forming aircraft body panels. J. Manuf. Syst. 17, 287–296. doi:10.1016/S0278-6125(98)80076-9